Faculty and Researchers   Faculty and Researchers' Publications

Observations of Air-Sea Momentum Flux Variability Across the Inner Shelf

Ortiz-Suslow, David G.; Haus, Brian K.; Williams, Neil J.; Graber, Hans C.; MacMahan, Jamie H.

AGU Publications

RESEARCH ARTICLE

Observations of Air-Sea Momentum Flux Variability Across the Inner Shelf

David G. Ortiz-Suslow[1] (ID), **Brian K. Haus**[2] (ID), **Neil J. Williams**[2], **Hans C. Graber**[2] (ID), and **Jamie H. MacMahan**[1] (ID)

[1]Naval Postgraduate School, Monterey, CA, USA, [2]Rosenstiel School of Marine and Atmospheric Science, University of Miami, Miami, FL, USA

Abstract Over the open ocean, the aerodynamic drag coefficient is typically well predicted; however, the impact depth-limited processes have on the drag remains underexplored. A case study is presented here where winds, waves, and currents were simultaneously observed from a mobile platform that repeatedly transected the inner shelf of Monterey Bay, CA. Eddy covariance-derived drag coefficients were compared to several bulk parameterizations, including all of the roughness variations of COARE 3.5 and two explicitly depth-limited models. The analysis demonstrated that the drag was underestimated by $O(2\,\text{–}\,4)$ times and the variability with wind speed or cross-shore distance was not well predicted. The drag based on a recent depth-limited roughness length model performed substantially better than the rest of the bulk estimates, which were all within 15% of each other and effectively equivalent given typical operational uncertainties. The measured friction velocity was compared to a wave-dependent parameterization and generalizing the model to arbitrary water depth significantly improved the mean observation-model difference to within 30%. Latent variability in the observation-model comparison was associated with stability, wind direction, and wave steepness. The wind stress angle variability was also analyzed. Stress veering was correlated with the alongshore surface current within 2 km from shore ($r^2 = 0.7\,\text{–}\,0.95$, $p < 0.05$); offshore of this margin, consistent wind stress veering was observed and may be attributable to a secondary, low-frequency swell system. These results demonstrate that it remains a persistent challenge to accurately predict wind stress variability in the nearshore, especially at locations with complex wave and current fields.

Plain Language Summary As the wind blows over the ocean surface, the atmosphere experiences friction, or drag, as the air and water molecules interact. Small waves increase the *roughness* of the surface, which augments the drag felt by the atmosphere as the air flows over the waves. This physical interaction between atmosphere and ocean facilitates the exchange of energy and material (e.g., gas) across the ocean surface, as well as drives upper ocean currents. In the presence of large waves, or swell, this interaction becomes more complicated. The impact swell has on the atmosphere changes as these large waves travel into shallow water, thereby growing taller and steeper, however our understanding of this process is limited. We present an observational study that took place within Monterey Bay and our results suggest that typical models used to predict the ocean surface drag do not perform well in the nearshore zone. In fact, applying a *shallow* water model did not significantly improve model-observation comparison. We demonstrate that the mechanisms that characterize air-sea interaction in deep water, may not apply near shore. While coastal zones are limited, compared to the global ocean, their impacts on and response to human activity are profound and should be better understood.

1. Introduction

The sheared flow within the marine atmospheric surface layer (MASL) applies a tangential stress to the ocean surface, which acts to vertically transfer momentum from the marine atmospheric boundary layer to the upper ocean. This mechanical interaction facilitates wind-wave development, near-surface transport, and mixing. In the case of very old sea (i.e., swell) or decaying wind, this mechanical transfer may reverse directions, transferring energy from the ocean to the atmosphere.

From classical turbulence theory, the tangential stress, τ, within a surface layer is proportional to the vertical gradient of the mean flow, U (Tennekes & Lumley, 1972),

$$\tau = \rho \nu_T \frac{\partial U}{\partial z}, \tag{1}$$

where ρ is the fluid density and ν_T is an eddy viscosity. In the MASL, the vertical wind gradient is typically unknown, thus a drag law is utilized:

$$\tau = \rho_a \, C_D \, U_z^2, \tag{2}$$

where a refers to air, z refers to some height above the surface, and C_D is the aerodynamic drag coefficient of the ocean surface. From early investigations of wind flow over water, it has been postulated that there should be a positive relationship between C_D and U (Charnock, 1955); subsequently, several field studies confirmed this for a range of U (e.g., Large & Pond, 1981; Smith & Banke, 1975; Smith, 1980, 1988). These efforts have evolved into more sophisticated algorithms that determine the relationship between the input wind speed and the effective C_D, while controlling for a host of environmental factors (Andreas et al., 2014; Edson et al., 2013). These algorithms are widely used across a diverse range of atmospheric and oceanographic studies in order to calculate the surface wind stress from the mean observed or modeled wind speed.

U is not the only parameter that can predict the observed C_D variability, as the local sea state has been shown to affect the drag coefficient (Donelan, 1990). Kitaigorodskii and Volkov (1965) was one of the first studies to directly argue that the surface roughness (specifically, the roughness discussed by Charnock, 1955) should be some function of the local developing waves. Subsequent measurements have confirmed that there is a relationship between the surface roughness (ergo the wind stress) and the sea state (e.g., Anctil & Donelan, 1996; Donelan, 1990; Geernaert et al., 1986). Drennan et al. (2003) found a strong relationship between the surface roughness and wave age by only including observations made during purely wind sea conditions. This work demonstrated that the *peak* waves referred to by Kitaigorodskii and Volkov (1965) were in the wind sea band, as opposed to the total surface gravity spectrum, which could include swell (or nonwind driven) waves. In some form, these findings have been incorporated into the modern algorithms (e.g., COARE 3.5; see Edson et al., 2013).

While equation (2) is convenient, there are several drawbacks to parameterizing τ using C_D. Foremost among these is that C_D oversimplifies the complex turbulent interactions at the interface and is strongly *flow* dependent. In other words, it is very challenging (if not impossible) to find a universal drag law that can be applied to the entire marine atmospheric boundary layer (Drennan et al., 2003). Over the open ocean, the presence of swell waves can cause the measured C_D values to diverge significantly from the bulk estimates, for the same U (Drennan, Graber, & Donelan, 1999; Potter, 2015; Rieder, 1997). For example, in light wind conditions ($U < 2$ m/s) it is evident that the net momentum flux may transition from downward to upward, that is, from waves to air (Grachev & Fairall, 2001; Högström et al., 2018). This leads to a negative drag coefficient (Kahma et al., 2016). In these conditions (i.e., low wind speed and fast waves), the waves can disrupt the turbulence spectrum (Drennan, Kahma, & Donelan, 1999) and force $\partial U / \partial z$ to be nonlogarithmic (Donelan, 1990; Smedman et al., 1999). These effects are a result of the extension of the wave boundary layer (WBL) — the portion of the MASL where wave-coherent stress, τ_w, is a significant portion of τ — beyond typical values of O(1) m (Janssen, 1989) and into common measurement space O(5–10 m). During these conditions, Monin-Obukhov Similarity Theory (MOST) will be invalid and correcting for nonneutral MASL stability may be futile (Högström et al., 2013).

Swell waves can even affect observations made outside of the WBL. Potter et al. (2015) made direct measurements of the drag coefficient in winds up to 27 m/s and observed a dip in the turbulence spectrum that coincided with the peak in the wave spectrum. The authors argued that these measurements were made outside the WBL and that this phenomena may be evidence of flow detachment from the dominant wave crests causing a reduction in the flux localized to the scale of the peak waves. These observations suggested a mechanism for wind-wave interaction, outside of the WBL, that may impact the observed drag coefficient, which is related to a turbulent velocity scale (or the *friction* velocity), u_* by

$$u_*^2 = C_D U_z^2. \tag{3}$$

The influence of swell on the air-sea momentum flux is further complicated by changes in the ratio of swell to wind sea energy, changes in the relative direction between swell and wind, and by the presence of mixed swell and wind sea systems (Potter, 2015). Högström et al. (2015) present a model for u_* that takes into account both wind sea and swell contributions to the total C_D. This model is discussed in further detail below.

The vast majority of the works reviewed here involved measurements made across the open ocean and, excepting relatively few studies, the role transition in the momentum flux from open ocean to nearshore has not been fully characterized. The convergence of wind, waves, and currents in a limited water column at a land boundary creates an all-together unique MASL, which may not be well described by open ocean measurements and theory. In particular, it has been observed that C_D in depth- and fetch-limited regimes differs significantly from open ocean values, at comparable wind speeds (Geernaert, 1988; Mahrt et al., 1996). In both the RASEX and NEAQS-04 field studies, offshore flow drove strong deviation from MOST and COARE, respectively. Vickers and Mahrt (1999) found that the dimensionless shear function (φ) was no longer uniquely defined by stability, in the case of offshore flow in both stable and unstable conditions. Grachev et al. (2018) investigated the effect of the air-land/sea boundary transition on φ using field data as part of the Coupled Air Sea Processes and Electromagnetic ducting Research east coast campaign (CASPER-East). In generally offshore winds, Fairall et al. (2006) found the observed C_D was O(1/3) COARE and only converged as U approached 10 m/s. Grachev et al. (2011) and Ortiz-Suslow et al. (2015) independently recorded strong enhancement of C_D around coastal waterways, approaching an order of magnitude higher as compared to the open ocean equivalent.

The field studies reviewed above indicate the degree of complexity when confronting the problem of coastal air-sea interaction. However, these works broadly considered the coastal zone as well as all having a primary focus on the impact of the land-sea boundary. Other recent field studies have attempted to investigate the specific role depth-limited waves, both in shoaling and breaking, have on the air-sea fluxes. Shabani et al. (2014) and MacMahan (2017) investigated C_D variability over the surfzone, both finding C_D to be O(2) times the expected, open ocean value during onshore winds. The latter study related this increase to surfzone foam coverage due to wave breaking. Zhao et al. (2015) built a shallow-water drag parameterization based on measurements made over the continental shelf, where waves were actively shoaling, that ranged from near-zero to typhoon wind speeds. They observed a roll-off in the drag (Donelan et al., 2004) at lower-than-expected U, which they attributed to shoaling-induced wave steepness. Ortiz-Suslow et al. (2015) reported on the spatial variability about a tidal inlet. In that study, C_D was not well predicted by bulk parameterizations near the inlet region, but tended to converge outside the inner shelf where nearshore processes had a limited impact.

Though these recent field studies provide key insights into coastal air-sea interaction relative to the open ocean, it remains a distinct challenge to directly relate the wind stress variance to contemporaneous variability in the underlying wave and current fields. This is largely due to a heavy reliance on tower-based measurements, which provide excellent temporal resolution but are inherently unable to capture the spatial evolution of these dynamics. There is a need to understand the cross-shore evolution of the air-sea interaction within the depth-limited nearshore environment. This was addressed to some extent by Anctil and Donelan (1996) and Ortiz-Suslow et al. (2015), but further investigation in the presence of shoaling swell waves is needed.

In order to help address these gaps, the Coastal Land-Air-Sea Interaction (CLASI) field program was undertaken to specifically examine the nature of air-sea interaction within the coastal environment. The program took place along the coast of the Monterey Bay (MB), California. A subset of the CLASI data will be presented here and the focus of this study will be on observations made from a heavily instrumented, small research vessel, which was able to simultaneously collect eddy covariance flux measurements, surface wave elevations, and current profiles. This study helps build upon recent coastal observations by detailing the evolution of air-sea interaction from the inner shelf to surfzone; this is critical to understanding how the wind stress field transitions from sea to land. Furthermore, this data set provides a case study for the effects a mixed and shoaling wave field has on the air-sea momentum flux. Gaining a more comprehensive understanding of the influence coastal processes have on the physical interactions between the atmosphere and ocean in shallow water will help to improve both observations and modeling of nearshore dynamics.

2. Theoretical Background

The flow within an incompressible, turbulent boundary layer can be modeled using the Reynolds-averaged Navier-Stokes (RANS) equation,

$$\rho \left(\frac{\partial U_i}{\partial t} + U_j \frac{\partial U_i}{\partial x_j} \right) = F_i + \frac{\partial}{\partial x_i} \left[-P\delta_i + \mu \left(\frac{\partial U_i}{\partial x_j} + \frac{\partial U_j}{\partial x_i} \right) - \rho \overline{u_i u_j} \right], \tag{4}$$

where the flow has been decomposed into the mean (U) and fluctuating (u) components. Equation (4) states that the total changes in momentum (left-hand side) are balanced by the mean body forces (F_i) and total stress divergence (square brackets; Tennekes & Lumley, 1972). In the MASL, this equation is substantially simplified by assuming that over the averaging interval of the mean there is stationarity, no external forcing, observations were made outside the viscous sublayer, and there is no mean pressure gradient. Outside of the WBL, the MASL can be modeled as a classical one-dimensional sheared layer and, following the original theories posed by Prandtl (1925), the vertical stress gradient disappears,

$$\frac{\partial \tau_{\text{total}}}{\partial z} = \frac{\partial \tau_{Re}}{\partial z} = 0, \tag{5}$$

and so the Reynolds stress, $\tau_{Re} = -\rho\overline{u_i u_j}$, is the total stress, τ_{total} and is constant. The bar here represents an appropriate averaging interval.

2.1. The Eddy Covariance Technique

Generally, the only components of the Reynolds stress tensor that are explicitly considered are the along- and across-stream covariance terms,

$$\tau = -\rho_a(\overline{uw}\hat{i} + \overline{vw}\hat{j}), \tag{6}$$

where u, v, and w represent the fluctuating components of the along, across, and vertical wind velocity, respectively. Note that the Reynolds stress will simply be referred to as τ (as in equations (1) and (2)). Using the full wind stress vector (equation (6)) enables defining a stress angle, θ_τ, that is independent of the mean azimuthal wind direction,

$$\theta_\tau = \arctan(\overline{vw}/\overline{uw}). \tag{7}$$

Equations (2), (3), and (6) can be rearranged to give the friction velocity in terms of the fluctuating velocity components,

$$u_* = (\overline{uw}^2 + \overline{vw}^2)^{1/4}. \tag{8}$$

The friction velocity is the turbulent velocity scale within the MASL and rewriting equation (1) to explicitly define ν_T, while taking into account equation (8),

$$\frac{\tau}{\rho_a} = u_*^2 = \kappa u_* z \frac{\partial U}{\partial z}$$
$$\frac{\partial U}{\partial z} = \frac{u_*}{\kappa z}, \tag{9}$$

where κ is the Von Kármán constant (taken as 0.4) and z is the measurement height in the MASL. Equation (9) gives the familiar flux-profile relationship for momentum, which can be integrated to yeild,

$$U - U_0 = \frac{u_*}{\kappa} \log\left(\frac{z}{z_o}\right), \tag{10}$$

where log is the natural logarithm and U_0 is the mean wind speed at the surface (generally assumed negligible, ; Potter et al., 2015). The parameter z_o is the surface roughness, or the height above the water surface where U → 0. Equation (10) gives the idealized wind speed at the measurement height z, but it has become standard to report the equivalent wind speed at $z = 10$ m. After applying this substitution,

$$U_{10} = \frac{u_*}{\kappa} \log\left(\frac{10}{z_o}\right), \tag{11}$$

which by expanding the logarithm in equation (10) can be rewritten in terms of the mean observed wind speed, U_z,

$$U_{10} = \frac{u_*}{\kappa} \log\left(\frac{10}{z}\right) + U_z. \tag{12}$$

From this, the C_D at 10 m becomes,

$$C_{D10} = \left(\frac{u_*}{U_{10}}\right)^2. \tag{13}$$

These formulae assume that the MASL is under neutral conditions, but it is well established that stability can affect the expected logarithmic wind profile. Monin and Obukhov (1954) used dimensional analysis to demonstrate that a scaling function should be applied to equation (9) to correct for these stability effects. The corrected relationships are

$$\frac{\partial U}{\partial z} = \frac{u_*}{\kappa z}\varphi(\zeta) \tag{14}$$

$$U = \frac{u_*}{\kappa}\left[\log\left(\frac{z}{z_o}\right) - \psi(\zeta)\right], \tag{15}$$

The empirical relationships for $\psi(\zeta)$ used in this study were those given in Donelan (1990) and Anctil and Donelan (1996).

2.2. Bulk Drag Coefficient Models

Numerous models exist for determining the air-sea exchange coefficients, that is, C_D (e.g., Large & Pond, 1981; Smith & Banke, 1975; Smith, 1988). The COARE 3.5 algorithm (Edson et al., 2013) is a comprehensive and widely used means of calculating the momentum and scalar fluxes, which is based on parameterizations developed from many field data sets. For the purpose of this study, the COARE 3.5 output will be considered the open ocean equivalent drag coefficient. Currently, COARE 3.5 supports three different methods for calculating the drag, based on variations in the Charnock coefficient (Charnock, 1955), which is used to calculate z_o. The

$$z_{o_1} = 0.0017\, U_{10} - 0.005 \tag{16}$$

$$z_{o_2} = 0.114\left(\frac{u_*}{C_p}\right)^{0.622} \tag{17}$$

$$z_{o_3} = 0.091\frac{H_s g}{u_*}\left(\frac{u_*}{C_p}\right)^2, \tag{18}$$

where H_s is the significant wave height, C_p is the phase speed of the peak waves, and g is gravitational acceleration. The coefficients given here are those from the COARE 3.5 algorithm. These z_o relations translate to three variations in the COARE-derived C_D: wind speed-only-dependent (equation (16)), wave age-dependent (equation (17)), and sea state-dependent (i.e., wave steepness; equation (18)). These three variations will be tested against the eddy covariance-derived C_D.

Drennan et al. (2003) investigated the dependence of the roughness length on wave age in swell and wind sea conditions using a compilation of data sets. Using field data, a wind speed-dependent, linear relationship for the drag coefficient was developed for *pure* wind sea conditions,

$$C_{D_{\text{wind sea}}} = 10^{-3} \times (A\, U_{10} + B), \tag{19}$$

where A and B are the linear coefficients 0.105 and 0.167, respectively (Högström et al., 2015). The CLASI observations are not expected to reflect pure wind sea conditions, but this model will be useful as baseline or control model. It should be noted that the COARE 3.5 algorithm was developed from open ocean data, but not necessarily pure wind sea conditions; therefore, differences between COARE 3.5 and Drennan et al. (2003) were expected.

Observations of momentum flux were made from a tower over the continental shelf in the South China Sea and were used to develop a drag coefficient that was explicitly a function of the water depth and wind speed (Zhao et al., 2015). The strategy for this study was to develop a parametric model that acknowledged the various drag coefficient regimes when considering wind speeds ranging from low to extremely high winds (i.e., typhoon conditions). The depth-limited drag coefficient was defined as

$$C_D = \max\left\{\frac{1}{b + \tanh(\alpha)^b}, \frac{\exp[-\beta]}{\tanh(\alpha)^b}\tilde{C}_D\right\}, \tag{20}$$

where b is 0.25, $\alpha = gd/U_c$, and $\beta = (U_{10} - U_{\text{ref}})^2/gd$. The parameter d is the water depth and U_c is assumed the maximum 10-m wind speed in deep water (Zhao et al., 2015 used the value of $U_c = 34$ m/s, from Donelan et al., 2004). U_{ref} is U_c scaled by a coefficient that relates the deep and depth-limited dominant wave steepness:

$$U_{\text{ref}} = \frac{U_c}{r}$$

$$r = \frac{k}{k_\infty}\sqrt{\frac{C_{g\infty}}{C_g}}. \tag{21}$$

Here k and C_g give the wave number and group velocity of the dominant waves, respectively (the latter is derived using linear dispersion). ∞ denotes deep water values. Finally, $\tilde{C}_D$ is defined as the quadratic relationship:

$$\tilde{C}_D = p_1 \tilde{u}^2 + p_2 \tilde{u} + p_3, \tag{22}$$

where $\tilde{u} = U_{10}/U_{\mathrm{ref}}$. Note that U_{10} is the observed, eddy covariance-derived neutral, 10-m wind speed. The p_{123} were determined empirically using least squares polynomial regression. This polynomial relationship was used by Zhao et al. (2015) to fit their observed distribution in high winds. While the full depth-limited model is presented here, the wind speed regime for CLASI (i.e., <10 m/s) precludes the second term in equation (20) from ever being applied.

Recently, Jiménez and Dudhia (2018) proposed a new $z_o(d)$ and, using a controlled numerical experiment, demonstrated that this improved wind speed forecasting in water depths from 10 m to 100 m. The lower limit was set by the authors to avoid the nonlinearity associated with wave heights approaching the water depth. Following the results from Jiménez and Dudhia (2018), $z_o(d)$ takes the empirical form:

$$\log_{10}(z_o) = b + S \times U_{10}, \tag{23}$$

where b is approximately -4.51 and S is the depth-dependent slope of $z_o(U_{10})$. S is well described by a power law,

$$S = B + M \log_{10}(z), \tag{24}$$

here B is 0.26018 and M is -0.085946. The empirical formulae above are based on the curves given in Figure 5 of Jiménez and Dudhia (2018). Therefore, given some d and U_{10}, one can derive a depth-dependent, 10-m neutral drag coefficient: $\sqrt{C_D} = \kappa / [\log\left(\frac{10}{z_o(d,U_{10})}\right) + \psi]$. For this bulk model, ψ was the same as used for correcting the eddy covariance estimates.

In summary, the parametric drag coefficients presented here provide a means of comparing the CLASI measurements to a state-of-the-art algorithm (COARE 3.5), a purely wind sea condition (Drennan et al., 2003), and two depth-dependent models of independent origins (Jiménez & Dudhia, 2018; Zhao et al., 2015). One of the primary goals of this study was to directly test if any of these parameterizations adequately capture the observed variability in C_D over this inner shelf region.

2.3. Wave-Dependent Friction Velocity Parameterization

The first two terms in equation (19) give the Reynolds stresses directly from the measured friction velocity. Högström et al. (2015) present a wave-dependent parameterization for u_* that accounts for the varying effects of swell and wind sea on the tangential and form drag (Donelan et al., 2012). The measurements presented in this article were used to test the results of this model in a nearshore environment. The formulation of this model is briefly presented here, but the reader is directed to this previous article for a more complete description of the theoretical basis.

The friction velocity proposed by Högström et al. (2015), u_{*H}, can be summarized as the balance of four terms:

$$u_{*H}^2 = (A_\tau + B_{\mathrm{form}})_{\mathrm{swell}} + (C_\tau + D_{\mathrm{form}})_{\mathrm{wind\ sea}}, \tag{25}$$

where the τ and *form* terms refer to the tangential stress and form drag, respectively; while swell and wind sea refer to the contribution at the peak frequency for each band of the surface gravity wave spectrum, respectively. For the form drag, the contribution from swell arises when the wind is traveling slower than the peak waves and results in net *upward* momentum flux, that is, water to air (cf. Högström et al., 2018). Collectively, the C and D terms in equation (25) are the *total* wind sea contribution and can be parameterized using a drag coefficient,
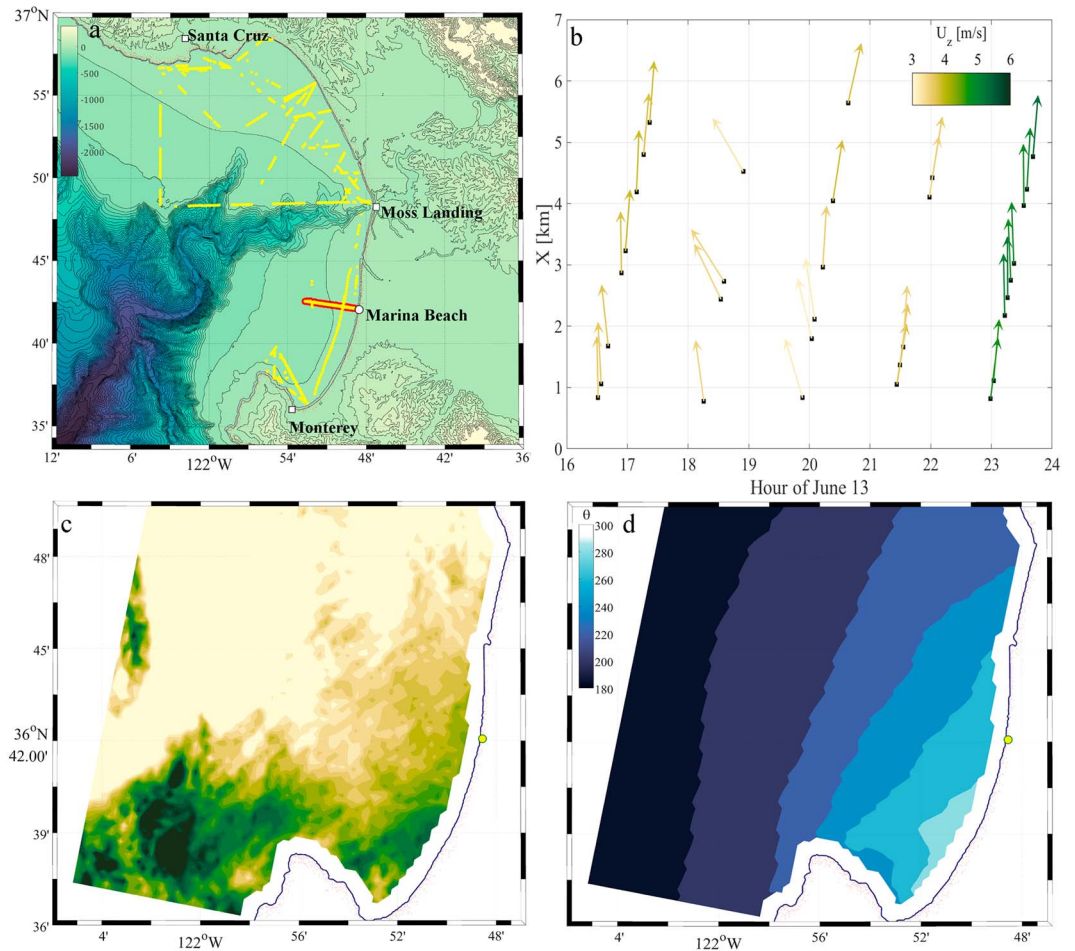
$$u_*^2|_{\mathrm{windsea}} = (C_\tau + D_{\mathrm{form}})_{\mathrm{windsea}} = C_{D_{\mathrm{windsea}}} U_{10}^2, \tag{26}$$

where $C_{D_{\mathrm{windsea}}}$ is the same as in equation (19).

The swell terms in Equation 25 are functions of swell significant wave height, H_{sd}, and swell peak frequency, f_{sp},

$$A_\tau = \beta H_{sd}^2 f_{sp}^2$$
$$B_{\mathrm{form}} = -u_*^2 (0.269 - 0.126 H_{sd}), \tag{27}$$

Figure 1. (a) Topographic map of the Monterey Bay region contoured with height above sea level in meters (National Geophysical Data Center, 2016); yellow points mark quality-controlled data observed during the CLASI experiment; the 13 June data set is highlighted in red. (b) Time-space diagram of the five cross-shore transects analyzed for this study, mean wind vectors are given along the transects (every third is shown for clarity). A SAR image (COSMO-SkyMed™) was acquired on 13 June at 02:06 UTC and from the roughness map the surface wind speed (c) and direction (d) were derived. The colors scale is the same in (b) and (c).

where β is a scaling coefficient with a value of 1.25. With these definitions, Equation (25) can be rewritten as,

$$u_{*H} = \sqrt{\frac{C_{D_{\text{windsea}}} U_{10}^2 + \beta H_{\text{sd}}^2 f_{\text{sp}}^2}{1.269 - 0.126 H_{\text{sd}}}},$$

(28)

which provides a model for u_* solely in terms of bulk wind and wave parameters.

Following equation (17) of Högström et al. (2015), the A_τ term is a form of the orbital velocity at the crest of the peak waves,

$$(A_\tau)_{\text{swell}} = \beta H_{\text{sd}}^2 f_{\text{sp}}^2 = \alpha c_0^2,$$

(29)

where α is another scaling coefficient that can be approximated as $\beta/5$ and c_0 is the orbital velocity at the crest. The development of u_{*H} is based on two important assumptions: (1) deep water, linear waves and (2) that the wave spectrum is composed of a wind sea and very narrow banded swell, such that the latter can be approximated as a monochromatic wave with carrier frequency f_p. In this study, the original form of u_{*H} will be tested against the CLASI measurements as well as a generalized form of u_{*H} that does not rely on assumption #1. Generalizing u_{*H} to arbitrary water depths has the largest implication for A_τ, where the orbital velocity at the crest of a wave in intermediate water becomes $c = c_0/\tanh(kd)$ (Holthuijsen, 2007; k is the wave number, here k_p was used, and d is the local water depth).
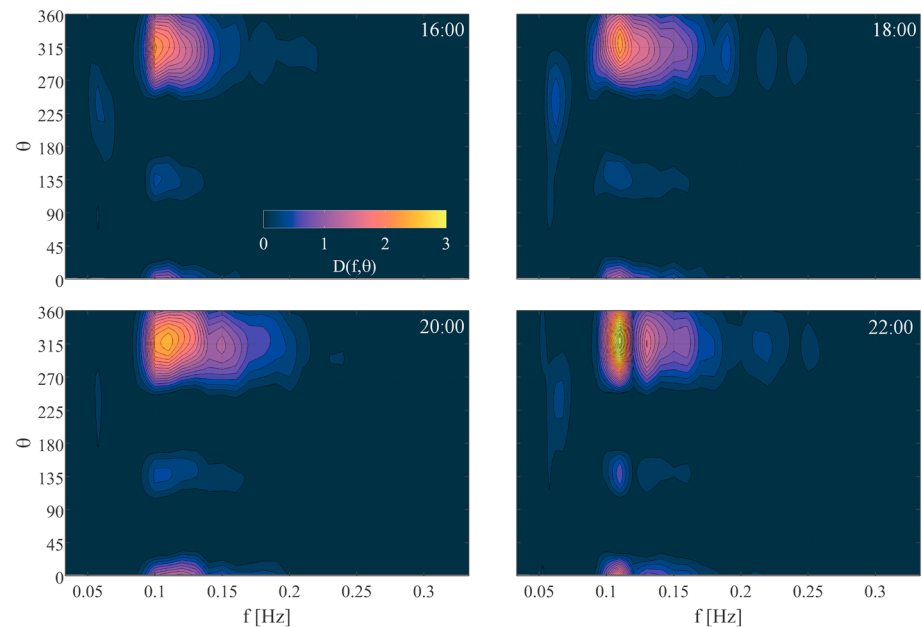
Figure 2. Directional wave spectra from the 3-m DISCUS buoy (NDBC 46042), moored 25 nautical miles due west of Moss Landing, observed over the course of the study period. Degrees are given in meteorological (coming from) convention.

3. Field Measurements

CLASI was a multiplatform effort to investigate the temporal and spatial scales of atmospheric forcing variability within the coastal zone. CLASI was conducted in MB, which lies along the Central California coast, from 7 to 16 June 2016. During this time, the wind and wave conditions varied significantly within MB and various case study data sets were collected as part of this field campaign. The present study work will focus on one such case study: an 8-hr period on 13 June from 16:20 to 23:55, during which time a small research vessel conducted repeat surveys offshore of Marina Beach.

3.1. Study Site

MB is a large, west facing embayment that is well-exposed to the wind and waves of the Northeast Pacific. The bay's eastern shore runs roughly north to south and is generally sandy with a relatively gradual slope, O(0.03); while the northern and southern coastlines run east-west and northwest-southeast, respectively (Figure 1a). These are characterized by bluffs, rock reef, and kelp forests. The regional bathymetry is largely defined by the Monterey Canyon, which bisects MB and terminates at Moss Landing and the mouth of Elkhorn Slough, a large tidal estuary. The measurements made for this case study were collected offshore of Marina Beach, which lies to the south of Moss Landing.

The conditions during the day of 13 June were fairly typical for the MB area during the late spring, early summer. The morning exhibited a strong marine layer with light wind. The marine layer eventually dissipated, coinciding with the development of a 6-m/s sea breeze in the afternoon (see Figure 1b). During the first half of the measurement period, the remnants of a strong southerly flow that had peaked within the previous 24 hr was observed. The fully developed *southern surge* was captured by a Synthetic Aperture Radar (SAR) image taken early in the morning of 13 June and SAR-derived wind fields showed that this flow was most intense in the southern half of MB. By the time of the measurements presented in this study, the intensity of this event had significantly diminished. The incident wave field to MB during 13 June included a combination of southwesterly and northwesterly swell systems in the 6- to 10-s band, though the latter was much stronger (see Figure 2). Also, long-period southwesterly swell, ~17 s, was present throughout the measurement period. These swell systems underlay the development of a distinct northwesterly wind sea that was driven by the diurnal sea breeze, which was strongest in the latter half of the sampling.

3.2. Data Collection and Processing

A 7.9-m long rigid-hull inflatable boat (RHIB) was instrumented with a suite of atmospheric and oceanographic sensors that provided simultaneous measurement of the wind, waves, and currents near the air-sea interface
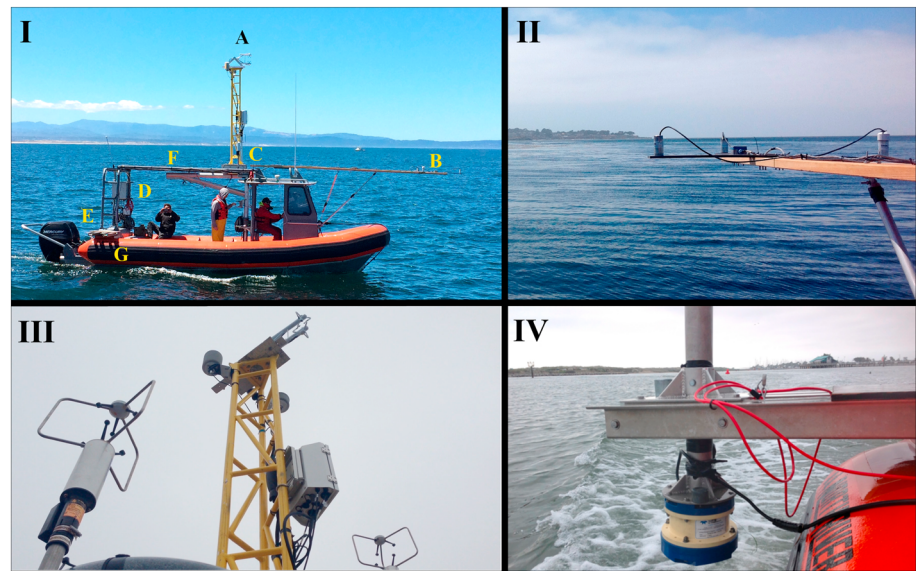
Figure 3. (I) The rigid-hull inflatable boat (RHIB) outfitted for this study: (A) Campbell Scientific IRGASON used for the eddy covariance measurements; (B) UDM triplet on the bowsprit; (C) two RM Young 3-D sonic anemometers mounted on the RHIB frame, both are situated in-line with the yellow mast along the port-starboard direction; (D) Campbell Scientific data logger enclosure; (E) accelerometers and rate gyros were mounted to the deck within a hold on the stern; (g) location of ADCP and CTD pole mount (not visible in this picture). (II) Close-up of the forward end of the bowsprit and the UDM triplet. (III) A view looking up at the RHIB's flux mast, with the lower RM Young anemometers visible beneath. (IV) Close-up of the ADCP and CTD (red cable) mounted on the pole mount and stowed out of the water for transiting.

(Figure 3). The RHIB was outfitted with a 2-m meteorological mast that was topped with a Campbell Scientific IRGASON flux system. The mast was rigidly mounted onto the RHIB superstructure and also held bulk temperature and relative humidity probes. In addition to the IRGASON flux system, two supplementary 3-D sonic anemometers (RM Young) were mounted on poles and fastened to the RHIB cage next to the mast.

Surface elevations were measured with a Senix Ultrasonic Distance Meter (UDM) triplet mounted on a bowsprit that extended beyond the RHIB hull and the bow wake (when traveling at sampling speeds). Currents were measured using a 1,200-kHz RDI Workhorse ADCP mounted in a downward orientation from a pole fixed to the starboard quarter of the RHIB. The ADCP head was approximately 0.75 m below the mean water line and the first bin was 1.3 m below the mean water line; a bin width of 0.25 m was utilized. Colocated with the ADCP was an independent (Decagon CTD-10) probe. A motion package (Columbia Research accelerometers and Systron Donner rate gyros) was rigidly mounted in an enclosure on the aft deck of the RHIB. The flux systems were acquired via Campbell Scientific data loggers, which was time synced via GPS link. The proprietary ADCP acquisition system was also synced to the local NTP server on the RHIB. All data, except GPS and CTD (1 Hz), were continuously sampled at 20 Hz. The ADCP acquired profiles at 2.11-s intervals.

The sampling strategy for 13 June was to perform repeat passes along an east-west transect extending from outside the surfzone to ~5 km due west of Marina Beach. This survey was conducted continuously from 16:20 through 23:55 UTC and with a vessel transit speed of under 1.5 m/s, each leg of the transect took about 1 hr to complete. A total of five westward legs and four eastward legs were completed. The focus of this study will be on the westward legs, because for these directions the RHIB was traveling into the wind, minimizing the potential effects of flow distortion. The RHIB and instrumentation design was conducive to making relatively undisturbed measurements of wind, waves, and currents when the vessel was pointed into the mean flow direction. Given the sampling strategy, a 5-min averaging interval was used for all eddy covariance processing. This window length is shorter than typical values (15–30 min), but was necessary here given the balance between temporal and spatial resolution. Similar arguments were made in Ortiz-Suslow et al. (2015) and this 5-min window effectively high-pass filters the MASL measurements. Successive 5-min windows were separated by 1 min. Over this window, the motion correction algorithm described in Anctil et al. (1994) and Drennan et al. (1994) was used for the flux and wave processing. An example of a successfully processed sample is given in Figure 4a.
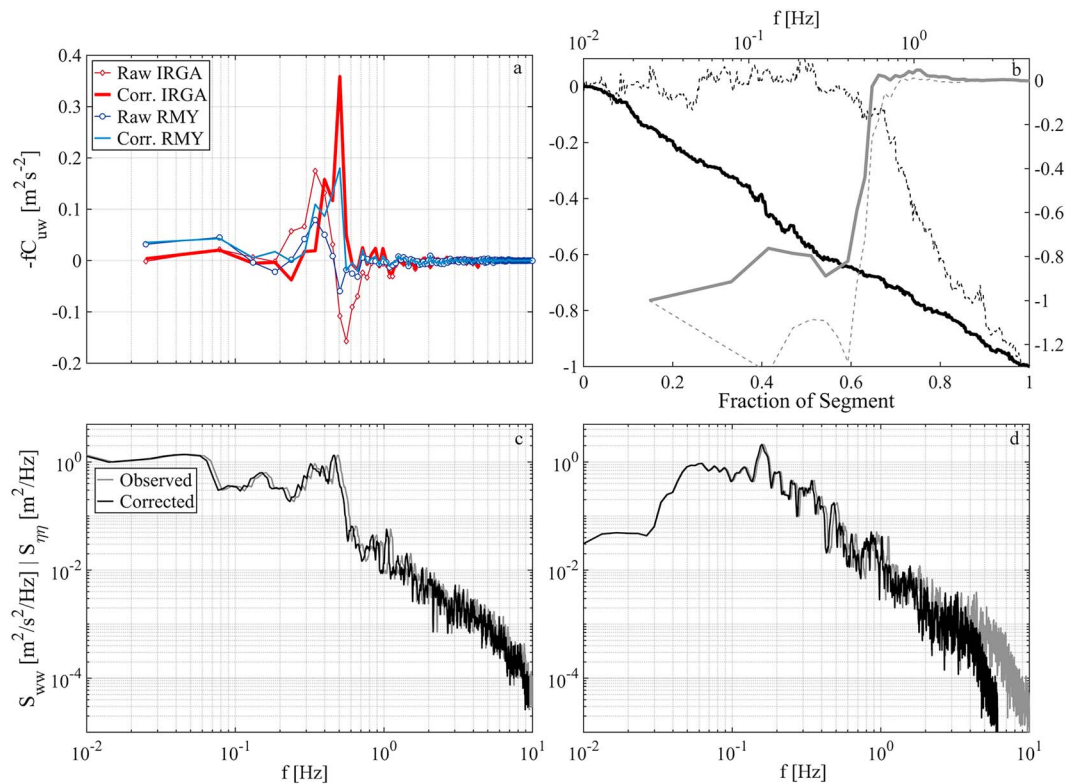
Figure 4. (upper left) Raw and motion-corrected, frequency-normalized covariance spectra from both the IRGASON and one of the RM Young sonic anemometers. (upper right) Normalized cumulative summation of the along-wind covariance (left axis) and the corresponding ogive (right axis), curves that pass (thick black/gray), and failed (dashed black/gray) quality control. (lower panels) Comparison of the observed (gray) and Doppler-corrected (black) autovariance spectra for the vertical wind velocity (left) and the surface elevation of the forwardmost UDM (right).

Several quality control steps were taken for each segment of data. Five-minute windows where the vessel heading deviated more than 30° were not included in the final data set. The raw flux-relevant parameters were screened using an adaptive Gaussian filter and flagged records were removed and interpolated using a polynomial. The surface elevation data were screened using a Goring and Nikora (2002)-type algorithm. A polynomial, rather than spline, was used to interpolate rejected records, because the spline was found to respond unrealistically to gaps. All of the 5-min segments that passed the automatic quality control steps were individually inspected for flux stationarity. This was done by visually inspecting the cumulative sum of the covariance between u and w and the ogive of the cospectrum. The cumulative sum was considered acceptable if it was approximately 1:1 for the entire record; and the ogive was accepted if it smoothly asymptotes to $|1|$ at low frequencies. Nonstationary segments were removed from the final data set (Figure 4b). Also, Doppler correction was applied to the observed wave height following Collins et al., 2017 (2017; Figures 4c and 4d). This had the most significant affect >1 Hz, due to the slow translation of the RHIB.

4. Results

The case study presented here focused on repeated surveys along a transect spanning from just outside the surfzone of Marina Beach to ~5 km offshore; none of the measurements presented here were made over the surfzone. This subset of the CLASI data is presented here, because the sampling was optimal for capturing both the spatial and temporal variability of the air-sea momentum flux. While this study only includes ~8 hr of observations and the range of C_D and u_* was limited, the variability in the momentum flux was representative of the entire CLASI program (Figure 5).

On 13 June, the observed wind speed, U_z, ranged from 3.5 to 7.5 m/s, increasing during the first half of the observations and then tending to level off by 23:00 UTC (Figure 6). The wind direction was generally observed to be westerly (260–280°), except for the hours of 17.5–20, when a nearly 30° southerly shift in the wind was observed.
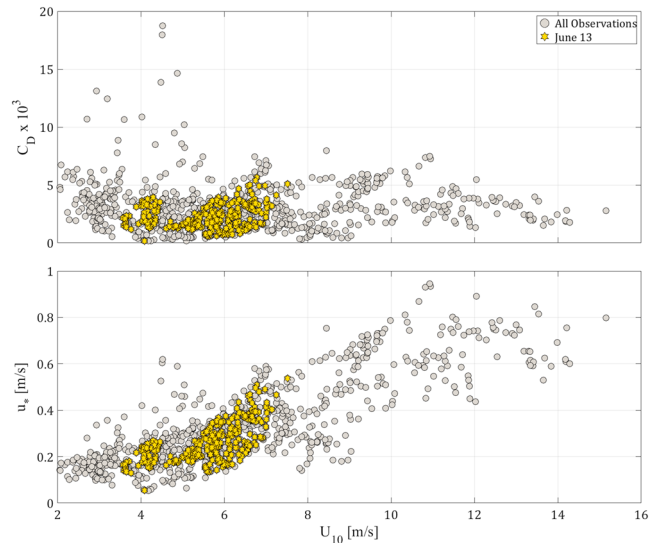
Figure 5. The eddy covariance-derived momentum flux parameters, C_D (top) and u_* (bottom), for all of Coastal Land-Air-Sea Interaction shown as a function of U_{10}. The 13 June data are highlighted. C_D is the 10-m, neutral equivalent.

Therefore, the wind was approximately onshore during the entire sampling period. This shift in wind direction was believed to be the remnants of the southern surge into MB that was captured several hours earlier by SAR (Figures 1c and 1d). Over the course of the entire measurement period, the MASL was observed to be unstable ($-0.2 < \zeta < 0$) and maximum air-sea temperature differences of nearly -4 °C were observed. The atmospheric stability trended toward neutral conditions as the day progressed, which was noted to coincide with the dissipation of the marine layer. The RHIB-observed waves showed an increasing H_s from under 1 m to just under 2 m, but the average wave period was a nearly constant 5.5 s throughout the day.

On 13 June, the directional wave spectra from the offshore NDBC buoy revealed several distinct energy sources (Figure 2). While directional wave information was not derived from the UDM triplet on the RHIB, each omnidirectional spectrum was partitioned into three bands: $f < f_s$, $f_s < f < f_c$, and $f > f_c$, where f_s was set to 0.08 Hz (Figure 6). The wind sea-swell cutoff frequency, f_c, was determined following Potter et al. (2015):

$$f_c = \frac{g}{2\pi 1.2 U_{10}}, \qquad (30)$$

here g is the gravitational acceleration, 9.81 m/s². The total fraction of energy across the three bands was determined by integrating the Doppler-corrected omnidirectional wave spectra,

$$E_{ab}/E_{TOT} = \frac{\int_a^b S(f)df}{\int_0^\infty S(f)df}, \qquad (31)$$

where a and b are the cutoff frequencies. The three fractions can be considered representative of the low-frequency swell, midfrequency swell, and the wind sea bands. Linear regression was used to test if an

Table 1
Conceptual Summary of Bulk Relationships Used for the R^i_{CD} Analysis

i	Equation	Dependence	Source
1	(16)	U_{10}	Edson et al., (2013; *COARE 3.5*)
2	(17)	u_*/C_p	Edson et al., (2013; *COARE 3.5*)
3	(17)	$u_*/C_p^{windsea}$	Edson et al., (2013; *COARE 3.5*)
4	(18)	$u_*/C_p, H_s$	Edson et al., (2013; *COARE 3.5*)
5	(19)	U_{10}	Drennan et al. (2003)
6	(20)	$\frac{k}{k_\infty}\sqrt{\frac{C_{g\infty}}{C_g}}, U_{10}, d$	Zhao et al. (2015)
7	(23)	U_{10}, d	Jiménez and Dudhia (2018)
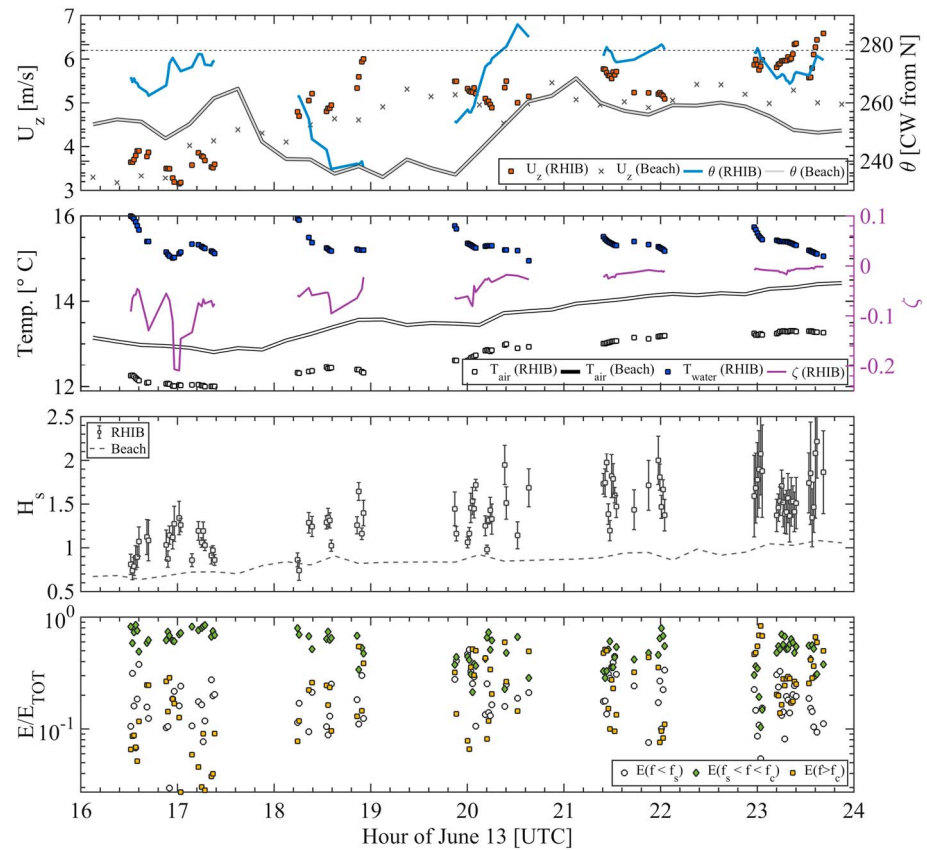
Figure 6. Overview of case study data set analyzed for this work. From top to bottom, the wind speed and direction (right axis), air-sea temperature and stability (right axis), significant wave height, and the fraction of total wave energy segregated into three subbands. The measurements made from the Marina Beach and surfzone station are provided (in some cases) for comparison. Each clump of data that represents a transect and progression in time corresponds to westward translation.

overall trend was captured transect to transect. The low-frequency band made up 19.34% of the total energy and did not exhibit a significant trend ($p = 0.489$) over the course of sampling. The midfrequency swell contributed the majority of the wave energy, but was found to significantly decrease ($r^2 = 0.289$, $p < 0.001$) in relative contribution from 69.81% to 47.01%. This decrease over the midfrequency swell band, coincided with a significant increase ($r^2 = 0.243$, $p < 0.001$) in the wind sea energy, 11.34% to 34.86%. The general environmental conditions for 13 June reflect a very dynamic and complex air-sea interface across this inner shelf region.

4.1. The Drag Coefficient

The observed air-sea momentum flux from the RHIB during 13 June was fairly typical of MB during the CLASI campaign (Figure 5) but was found to be almost exclusively higher than various bulk parameterizations, for a given wind speed (Figure 7). The eddy covariance technique allows for directly estimating C_D, which is the most widely used means of representing and calculating the surface wind stress over the ocean, both in models and observations. In order to facilitate comparing the observed and parameterized drag, the R_{CD} ratio will be defined:

$$R_{CD} = \frac{C_D^{eddy}}{C_D},$$
(32)

which is similar to the ratio defined in Ortiz-Suslow et al. (2015). Here C_D will refer to a drag coefficient determined from a bulk relation model, for example, COARE 3.5 (Edson et al., 2013) and *eddy* refer to the directly observed drag coefficient from the RHIB's flux tower. Because so many different methods for calculating R_{CD} were used, each variation will be assigned a number and they will be referred to as R_{CD}^i (see Table 1). For R_{CD}^2 and R_{CD}^3, the wave age (u_*/C_p) was calculated using the peak phase speed, C_p, over the entire wave spectrum
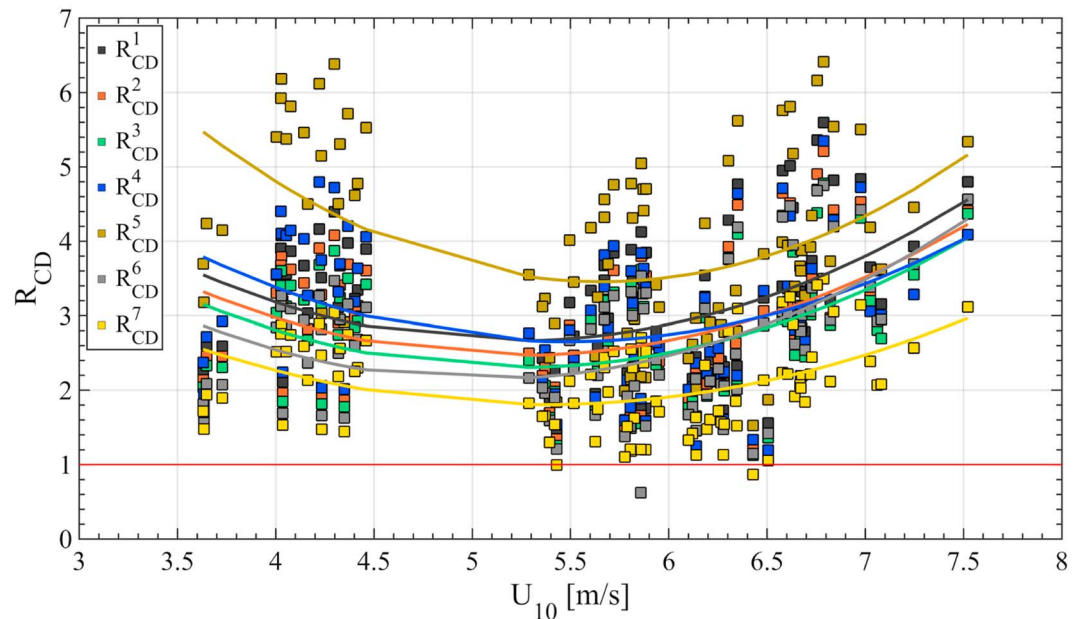
Figure 7. R_{CD} as a function of U_{10} for the various bulk parameterizations and models tested. The codes for the versions 1–7 are given in Table 1. The solid lines show quadratic fits to each distribution, respectively. A value circa 1 indicates observation-model agreement.

or for only the wind sea band, respectively. For R_{CD}^4, the total C_p was used. An R_{CD} value of 1 signifies that the bulk model in question matches the observations and thus accounts for the various environmental effects on C_D. In this regard, R_{CD}^5 is never expected to approach unity.

Generally, Figure 7 reveals that all of the R_{CD} versions were consistent in order of magnitude and overall U_{10} dependence. Across the seven variations, the mean R_{CD} ranged from 2.09 to 3.96. In other words, the directly measured wind stress across all transects was found to be approximately 2–4 times larger than would be expected by any bulk parameterization. While there are some significant differences across the various methods, the results demonstrate that no model was representative of the observed drag. In fact, there were only 11 samples that were within ±20% of C_D^{eddy} (i.e., $0.8 < R_{CD} < 1.2$), which represents less than 2% of the entire distribution. Of these 11 samples, seven were from R_{CD}^7 (the Jiménez & Dudhia, 2018 z_o model).

A series of 21 unique t tests were conducted to determine any statistically significant differences across the seven models. The tests assumed unequal variance and to satisfy the Gaussian distribution requirement of a t test, all inputs were normalized using methods presented in Niaki and Abbasi (2007). The α level (typically 0.05) was adjusted to account for anticipated multiple comparison issues and was set to 0.0024, or $\alpha = 0.05/21$. To determine if the results of the t test were dependent on changes to wind forcing, the series of tests were run again only for <SPI-I200» 5 m/s. The results of both sets of tests are summarized in Table 2.

As expected, the mean R_{CD}^5 was significantly higher by 20–45% when compared to the other estimates of C_D. Interestingly, the only exception was when comparing R_{CD}^5 to R_{CD}^6 (the explicitly depth-dependent parameterization) for $U_{10} > 5$ m/s. For this case, though the mean percent difference was 28%, the distributions were not found to be significantly different; this was attributed to the high variance of R_{CD}^5, which was 48% higher than the variance for R_{CD}^6. The measurements for $U_{10} > 5$ m/s tended to come from later in the day when the sea breeze had developed wind sea ($H_s \sim 1$ m) on top of the underlying swell systems.

The variations in COARE 3.5 tested, R_{CD}^{1-4}, were generally within ~10% of each other, and there was no particular variation that clearly performed better relative to the measured C_D. No significant difference was found when comparing the wind speed only (R_{CD}^1) and total peak wave age-dependent (R_{CD}^3) versions of the algorithm. When compared to the R_{CD}^6 parameterization, COARE 3.5 tended to be significantly higher by approximately 10%, for all wind conditions. R_{CD}^3 was found to be significantly higher than R_{CD}^6 for all tests, but in absolute terms the means were within 3%.

Table 2
Results of T-Tests for R^i_{CD} Parameterizations

	R^1_{CD}	R^2_{CD}	R^3_{CD}	R^4_{CD}	R^5_{CD}	R^6_{CD}	R^7_{CD}
R^1_{CD}	—	—	—	—	—	—	—
R^2_{CD}	7.23** (7.44)	—	—	—	—	—	—
R^3_{CD}	12.6* (12.8)	5.77*** (5.79)	—	—	—	—	—
R^4_{CD}	2.88*** (5.69***)	− − −4.61*** (−1.79***)	−11.2*** (−8.23***)	—	—	—	—
R^5_{CD}	−27.8*** (−20.7***)	-37.8*** (−30.5***)	−46.3*** (−38.6***)	−31.9*** (−28.8***)	—	—	—
R^6_{CD}	14.9 (13.3***)	8.28 (6.29***)	2.65*** (0.528***)	11.5*** (7.31)	32.5*** (28.0)	—	—
R^7_{CD}	32.5 (33.7***)	27.2** (28.3***)	22.7 (23.9***)	30.1*** (29.2***)	46.8*** (45.0***)	19.6 (22.4***)	—

Note. Values indicate mean percent difference relative to top row, for example, $100 \times (R^1_{CD} - R^2_{CD})/R^1_{CD}$, those in parentheses ( ) are for $U_{10} > 5$ m/s. Significant differences are noted: * $p \leq 0.1$, ** $p \leq 0.05$, *** $p \leq 0.001$.

R^7_{CD} presented a departure from the consistent underestimation of the drag. The total mean R^7_{CD} was 2.087 ± 0.6203 (1 standard deviation), which was 27% and 41% lower in the mean and variability relative to R^6_{CD} (the next lowest), respectively. Barring a few exceptions, and only from including the low wind data, the Jiménez and Dudhia (2018) z_o-derived C_D generally performed the best in comparison to all the other parameterizations tested against the CLASI measurements.

Thus far, the 13 June data have been considered in aggregate or, in other words, the R_{CD} distributions have been collapsed onto a single function U_{10}. This assumes that the various bulk parameterizations were able to account for all other sources of variance and that the residual dominant driver of R_{CD} variability should be wind speed. As expected within the nearshore and from Figure 7, this was not the case. Figure 8 presents a similar representation of the R_{CD} as a function U_{10}, but now separated by transect. A linear regression was done on each transect cluster and this was then compared to the overall quadratic relationship fitted to the collapsed data (using R^1_{CD} as representative). The collapsed data trend tended to diverge from the transect-by-transect regressions, for each sample variation. Essentially, the wind speed dependence observed for a single transect did not match the aggregated dependence on U_{10}. For example, during transect **I**, all variation in R^i_{CD} (except $i = 5$) exhibited a significant positive relationship with U_{10} ($p < 0.05$, except for R^7_{CD} $p = 0.06$); while for transect **V**, no significant trend between any R^i_{CD} and U_{10} was found.

Other than wind speed, cross-shore distance would intuitively seem to help explain R_{CD} variance. However, a high degree of intertransect and intratransect variability was found, and no consistent underlying pattern could be discerned simply via inspection (Figure 9). This lack of clear and consistent spatial dependence was found for all of the R_{CD} variations, though only 3, 6, and 7 are shown in Figure 9. This would suggest that some forcing not typically taken into account by the bulk parameterizations was responsible for the cross-shore variability. The observed spatial variability does not appear to be random, and fairly coherent trends were observed, albeit strongly nonlinear in some cases.

4.2. The Friction Velocity

C_D is a critical air-sea parameter that is derived from various theoretical relationships and empirically determined coefficients and thus is influenced by numerous factors. Most notably are the stability corrections used to account for nonneutral stratification in the MASL (equation (14)). There are various forms of these relationships and furthermore, some investigators have suggested that the logarithmic boundary layer assumption does not hold in the presence of swell waves (Högström et al., 2013), which invalidates MOST and the subsequent corrections. In order to circumvent this seemingly intractable problem, an independent investigation of the momentum flux was done on the variability in friction velocity (equation 8). the parameter u_* is essentially the directly measured momentum flux at the height of the sensor above the ocean surface and is independent of the majority of the assumptions incorporated into the C_D calculation.

The observed u_* was compared to u_{*H} using a ratio, similar to R_{CD}:

$$R_* = \frac{u_*^{\text{eddy}}}{u_{*H}}. \tag{33}$$
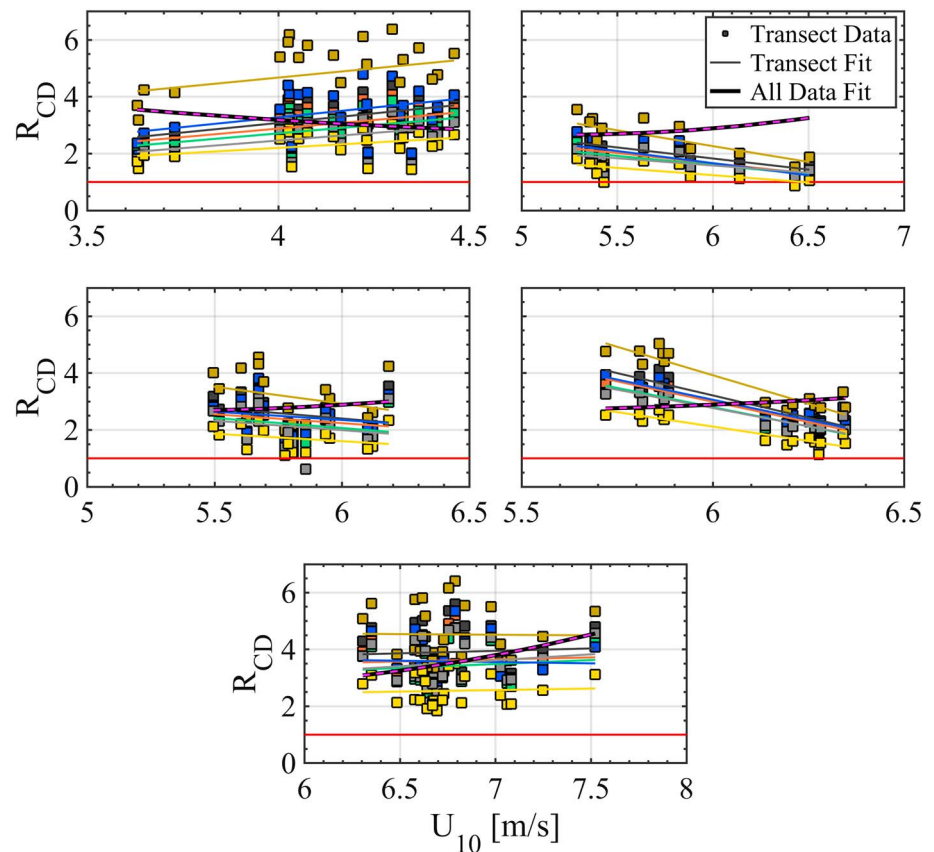
Figure 8. Same scheme as Figure 7, but now each transect is shown separately. The solid colored lines represent linear fits to the transect data, the thick black line shows the quadratic fit from Figure 8 for R_{CD}^1, over the appropriate wind speed interval.

Two versions of u_{*H} were used for comparison: (1) the original model presented in Högström et al. (2015) and (2) a version generalized to arbitrary water depths. The observed u_* was on average 1.529 ± 0.352 times larger than the modeled value, but this decreased by 11.9%, to 1.366 ± 0.289 for R_*^2. This also corresponded to a drop in variance by 22.2% between R_*^1 and R_*^2. These mean differences were found to be significant ($p = 0.0016$).

4.3. Multiple-Regression Analysis

R_* demonstrated that generalizing u_{*H} to account for depth-limited wave effects increased model-observation agreement, but strong intertransect variability persisted (Figure 10). Figure 11 summarizes the change in model-observation agreement with time, which demonstrates that there are three transitions in R_*:

1. a decrease toward unity from transects *I* to *II*;
2. followed by an increase from *II* to *III*;
3. and finally a further increase between *III* and *V*.

The transitions were found to represent significant differences in the mean R_* (for R_*^1: $p = 0.02$, 0.009, and 0.002, respectively) over the entire observation period. Interestingly, both the original and generalized forms of u_{*H} exhibit similar latent variability, but accounting for the depth-limited effects on the waves did decrease the divergence between the observed and modeled u_*, for each transect, respectively. This was especially true for transects *III* and *IV*, where R_*^2 was significantly lower than R_*^1 in both cases ($p < 0.005$). R_*^2 was ≤ 1.3 for all transects, except *V*, which represents fairly good model-observation agreement when compared to the level of divergence found for C_D.

Table 3
Results of Multiple Regression on R_*^2

X	C	SE
$I-II$, $r^2 = 0.785$		
ASTD***	3.518	0.6305
ζ***	−0.4522	0.09855
$a_s k_p$***	−4.578	0.8456
$b_{I,II}$	0.3142	0.3467
$II-III$, $r^2 = 0.5812$		
θ***	−0.01382	0.2307
ζ**	−0.26301	0.00217
$b_{II,III}$**	0.6513	0.2306
$IV-V$, $r^2 = 0.29817$		
θ_τ***	−0.6079	0.1379
Urs**	−0.03194	0.01491
$b_{IV,V}$***	1.659	0.0627

Note. C is the coefficient for each term in the model and SE is the standard error; r^2 is the adjusted coefficient of determination for the entire model; $b_{i,j}$ is the constant term. Significance indicated as: *$p \leq 0.1$, **$p \leq 0.05$, ***$p \leq 0.001$

The residual, mean variability observed in R_*^2 was investigated using multiple linear regression. The fundamental equation for a linear system with n predictors and m observations is

$$y^m = b + C_1 X_1^m + \cdots + C_n X_n^m, \tag{34}$$

where b is a constant. The goal of this analysis was to understand what processes drove the three major transitions in Figure 11. These represent three different periods of time for which the multiple-regression analysis was conducted (i.e., three subsets of m). The analysis was run independently for the three periods using all of the observations during the respective subsets. The analysis was conducted in this discrete manner, because it was hypothesized that the influence of specific processes may vary in time.

A total of 10 predictors were used to build the models, many of which have already been defined: (1) U_z; (2) wind direction (θ_z); (3) θ_τ; (4) air-sea temperature difference, ASTD; (5) ζ; (6) significant steepness (Collins, 2012),

$$S_s = \frac{2\pi H_s}{g T_{m_0}^2}, \tag{35}$$

where m_0 is the zeroth moment (i.e., mean) wave period (T); (7) peak wave steepness, $a_s k_p$; (8) peak wave age; (9) E_s; and (10) the Ursell number (Ursell, 1953),

$$Urs = \frac{a_s \lambda_p^2}{d^3}, \tag{36}$$

where λ_p is the peak wave length and a_s is the significant wave amplitude. The final parameter is an index of the nonlinearity of shoaling waves. The multiple-regression analysis was conducted iteratively to find a unique set of independent predictors whose coefficients were found to significantly contribute to the model
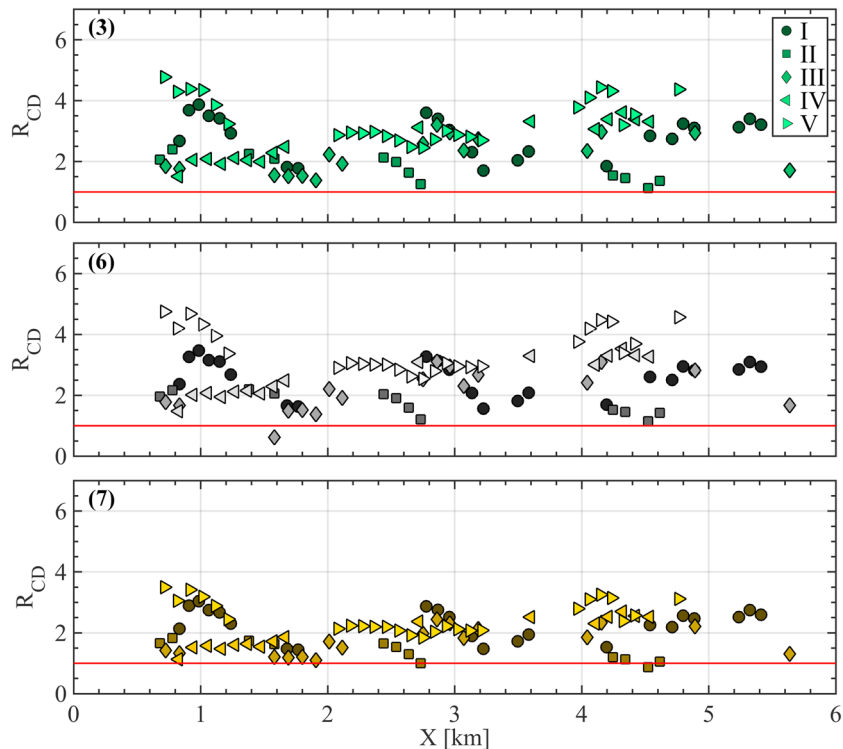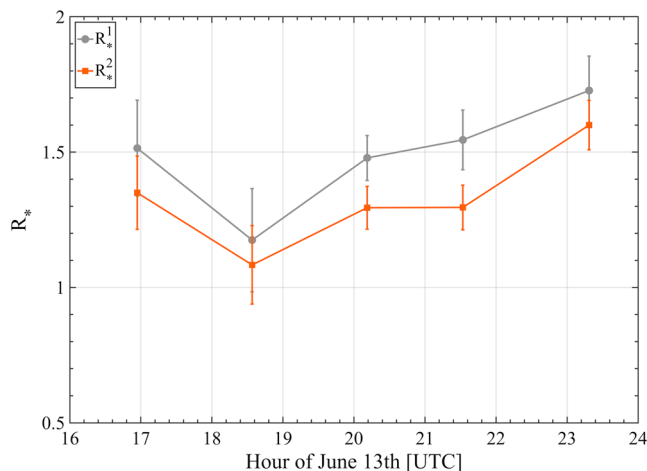

Figure 9. $R_{CD}^{3,6,7}$ as functions of cross-shore distance for all five transects (color shade).
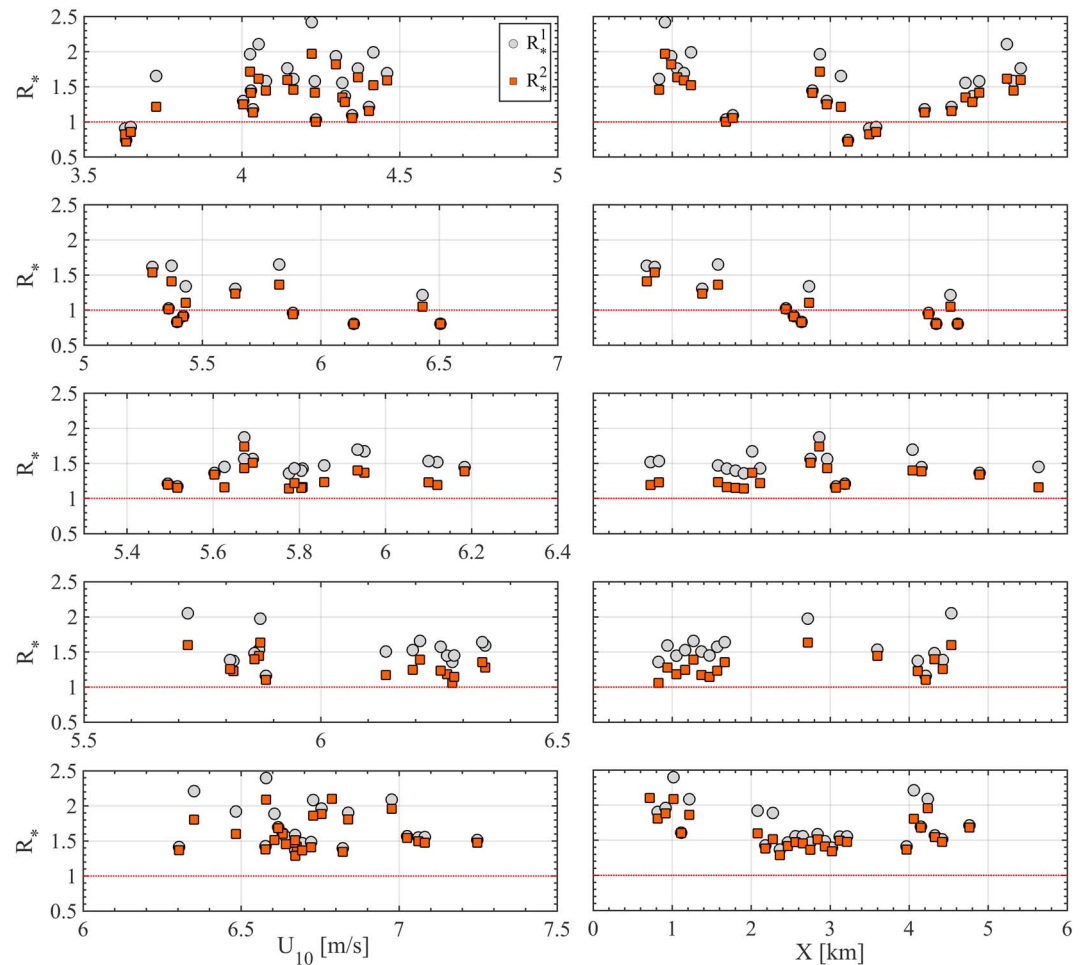
Figure 10. (left) R_* dependence on U_{10} for both the original Högström et al. (2015) model (1) and the modified version (2); (right) the dependence on cross-shore distance. From top to bottom, each row represents transects *I* through *V*.

($\alpha = 0.1$). Initially, for each of the three tests, any predictor exhibiting strong collinearity would be removed from the set.

A summary of the multiple-regression results is provided in Table 3. The transition observed from transects *I* to *II* was associated with changes in atmospheric stability (both ASTD and ζ) and wave steepness ($a_s k_p$); in particular, ASTD and $a_s k_p$ were the most influential factors in the model. The model results were fairly robust for this period and this set of predictors explained nearly 80% of the total variance over this time period. From *II* to *III*, the observed increase in R_*^2 could be largely explained (~60%) by changes in the observed wind direction as well as ζ, with the latter being the most influential predictor. Consistent with the period of *I* to *II*, R_*^2 was negatively correlated with ζ. Analysis of the transition from transects *III* to *V* provided relatively poor results, with a final set of predictors explaining < 30% of the observed variance. For this final test, θ_τ and *Urs* were found to contribute significantly to the regression model. The former was the most influential term apart from the constant term ($b_{IV,V}$). The relatively low performance of the model and high influence of the constant would suggest that this set of predictors did not contain the processes primarily responsible for the significant increase in R_*^2 observed between transects *IV* and *V*.

Figure 11. Comparison of the transect-mean for R_*^1 and R_*^2. The error bars span the 95% confidence interval (i.e., two standard errors of the mean).

Table 4
Linear Regression Results for Wind Stress Angle Versus Alongshore Surface Current Velocity

	N	r^2	N(X > 2)	$r^2(X > 2)$	N(X < 2)	$r^2(X < 2)$
I	23	0.0954	15	0.2309*	8	0.7243**
II	12	0.1505	8	0.2262	4	0.0403
III	17	0.3213**	12	0.3391**	5	0.9576**
IV	16	0.2472*	7	0.0177	9	0.8522***
V	26	0.0057	20	0.1006	6	0.0089

Note. N gives the number of samples per test; r^2 is the Pearson correlation coefficient, for each subset of X (significant correlations are noted: *$p < 0.1$, **$p < 0.05$, ***$p < 0.001$).

4.4. Wind Stress Veering

The variability of the wind stress angle relative to the mean azimuthal wind direction was also investigated. In comparison to C_D, the *actual* direction of the wind stress vector is largely overlooked, because in a mean sense it is typically assumed to be in-line with the wind vector. Also, most operational, coupled models do not directly resolve the wind stress components, but instead rely on the drag coefficient and wind speed to assign the ocean surface conditions.

Wind stress veering may arise from the relative directions between the surface currents and wind vector (Cornillon & Park, 2001), which has been linked to wave-current interactions (Ortiz-Suslow et al., 2015; Zhang et al., 2009). Grachev et al. (2003) extensively characterized the relationship between the wind stress angle and the relative angle between the wind vector and dominant swell wave directions. For CLASI, the variability of the wind stress angle was analyzed using the full wind stress vector (equation (7)) and the RHIB's ADCP. While local directional wave spectra were not resolved, the results are analyzed in the context of the incident, directional wave field (see Figure 2).

Over this portion of the MB inner shelf, the currents and waves are constrained by the local bathymetric variation, and therefore, the shore normal direction, $\theta_\perp$, was a natural reference. At Marina Beach $\theta_\perp$ was 278°, or almost due west. The azimuthal wind velocity and stress vectors, as well as the surface current vector, were all referenced to $\theta_\perp$ such that positive (negative) angles denote flow coming from the south (north) of the normal direction. Except for transect *II*, the wind velocity tended to be directly onshore, with a <20° southerly offset from $\theta_\perp$ (Figure 12).

Transect to transect, the wind stress angle exhibited a fairly consistent pattern of strong veering within 2 km of the shore, while offshore tending to converge on a constant angle with respect to $\theta_\perp$. This inner 2-km zone was associated with a significant change in the local water column depth (Figure 12). Offshore of 2 km, the mean wind stress angle across all transects, except *II*, was 26.2° ± 5.4° (1 standard deviation). Relative to the wind vector, this is a mean 22.2° ±3.9° veering southward. Transect *II*, was considered as separate case because the wind shifted substantially toward the south, resulting in a wind stress 55.1° south of $\theta_\perp$. Relative to the wind, however, the wind stress vector was only 16.4° off of the wind direction (Figure 12).

The wind stress angle was associated with the variance in the alongshore surface current velocities (Figure 13). On this day, the currents were observed to run north-south, with the flow magnitude ranging from 0.5 to 1 m/s. Therefore, for the entirety of the measurement period the currents were roughly perpendicular to the mean wind direction. For transects *I*, *III*, and *IV*, the variance in the wind stress angle was most strongly associated with the surface current variability within 2 km of the shore. For example, for *I*, across the entire transect only 9% of the variance in the wind stress angle was predicted by changes in the surface currents; however, this increases to 72.43% when only considering this 2-km margin closest to shore. This general trend was also observed for *III* and *IV* (see Table 4). Transect *II* did exhibit a trend similar to *I*, but this was not significant, which was due to too few samples within the 2-km margin. Transect *V* exhibited no relationship with the surface currents, though this cannot be linked to a lack or reduction in hydrodynamic forcing.

5. Discussion

The results presented here focused on three independent analyses: (1) an evaluation of the performance of several parameterized estimates of C_D with respect to an eddy covariance estimate; (2) a comparison of the
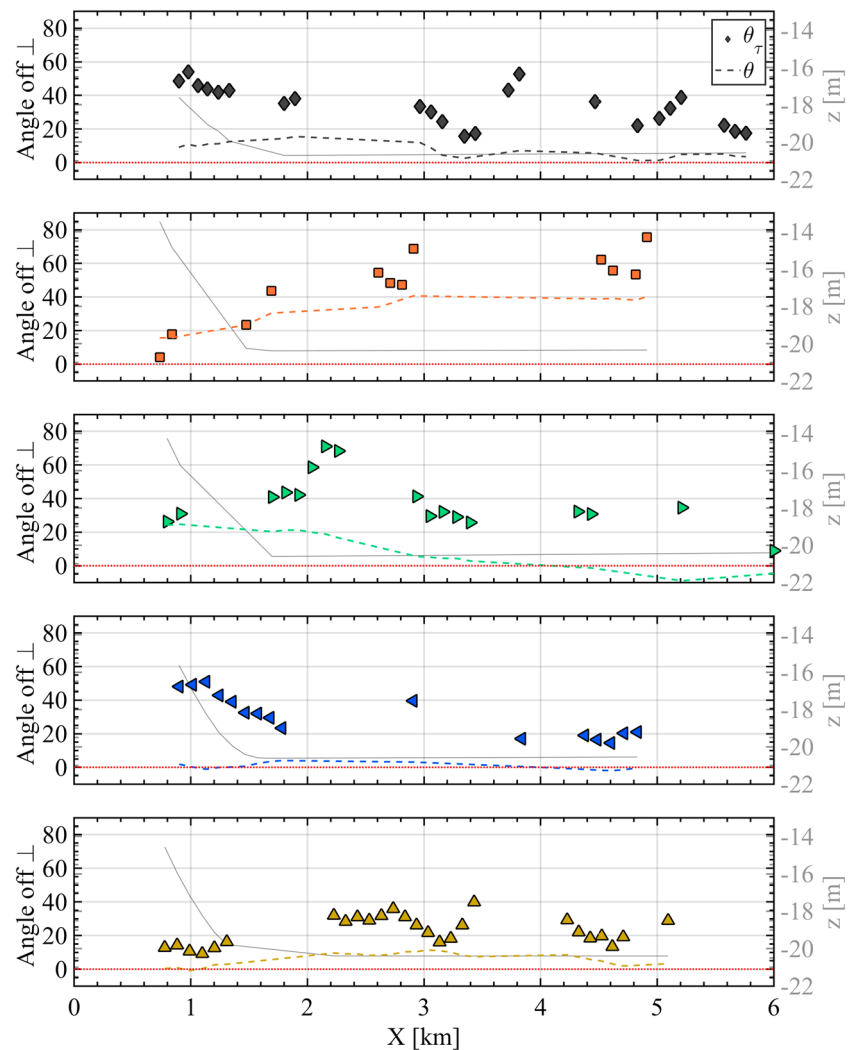
Figure 12. Azimuthal wind (θ) and wind stress (θ_τ) directions referenced to the shore normal ($\perp$), which for Marina Beach is 278°, for each transect *I* through *V* (top to bottom). Also, given in gray is the measured water depth, z, below the rigid-hull inflatable boat during the transects.

measured u_* to a bulk wave-dependent model; and (3) an investigation into the wind stress angle off of the mean wind direction. In conjunction, these three substudies represent a detailed case analysis of the air-sea momentum flux variability over the MB inner shelf. In more general terms, this work may be representative of nearshore systems with strong swell and mixed sea conditions.

The primary findings of the C_D analysis was that none of the models or parameterizations were able to sufficiently capture the measured variability. In a mean sense, the parameterized values underestimate the drag by O(2–4) times, though there was considerable spread (generally ±100%) about these means. Note that the entire CLASI data set comes from waves oblique (following) to the wind, which over the open ocean is typically associated with *reduced* drag (Kahma et al., 2016; Potter, 2015), but the measurements given here reveal *higher*-than-expected C_D. These findings would suggest that the mechanism governing drag reduction may be overwhelmed in the nearshore environment.

The R_{CD} intercomparisons revealed two fundamental results: (1) parameterizations relying on wave steepness did not perform substantially better than other wave-dependent models, and more generally (2) excluding R_{CD}^5 and R_{CD}^7, there was no effective difference between any of the drag models. The first point counters the conventional understanding for the mechanism driving C_D enhancement within the coastal zone. Namely, that wave steepening via shoaling should increase the roughness in a depth-limited water column (Jiménez & Dudhia, 2018). In more general terms, the second fundamental result highlights that all the various drag
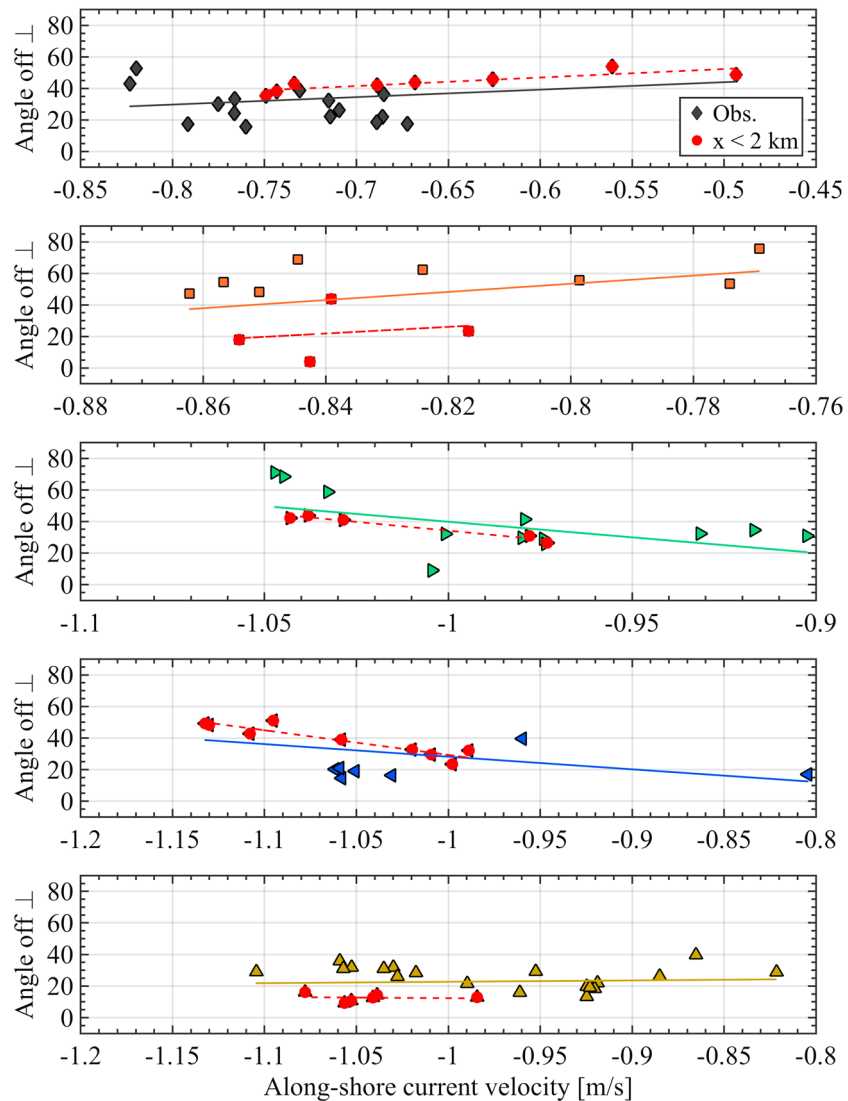
Figure 13. Wind stress angle relative to shore normal as a function of alongshore surface current velocity for each transect *I* through *V* (top to bottom). For the currents, values ≤ 0 indicate flow from the north of ⊥. The observations made within 2 km of the beach are highlighted in red. The solid and dashed lines give linear fits to the distribution for the complete and 2-km portion of the transects, respectively.

models were within 15% of each other. Operationally, this is within the expected uncertainty of any particular bulk parameterization as well as individual eddy covariance measurements. Effectively, for the CLASI data set, a wind speed-only-dependent drag (R_{CD}^1) would be just as effective as a sea state-dependent drag model (R_{CD}^4) or a depth-dependent drag model (R_{CD}^6). This finding suggests that even in a depth-limited environment, the role of the peak waves may be overstated in the presence of a wind sea of comparable intensity. The major exception to findings (2) was the depth-limited z_o-derived R_{CD}^7 proposed by Jiménez and Dudhia (2018), which was 20–30% lower than all the other models. While this model performed substantially better, it also failed to capture a significant portion of the measured variance. In particular, it could not reproduce the wind forcing dependence of the measured C_D, which suggests that the mechanism driving increased momentum flow in the nearshore is not fully understood.

The gap in understanding that the C_D analysis revealed was highlighted in the high intertransect variability captured in R_{CD}. Figure 8 demonstrated the differences between analyzing the dependence of R_{CD} as a collapsed function of wind speed and segregating the total data set by transect. In fact, the transect-based wind speed dependence tended to contradict the functional dependence of the data in aggregate. Therefore, the variability in the data cloud is not random variation about a mean, but the occluding of several trends within

one data set. For example, transect II exhibited a negative dependence with U_{10} ($r^2 = 0.58$, $p = 0.044$), whereas for transect V the relationship was nonsignificant. This finding points to a fundamental change in the dependence of C_D to U_{10} over a ~3-hr period. This suggests that perhaps in complex, nearshore environments it may no longer be valid to build empirical relationships for C_D that are functions of a single forcing variable, for example, U_{10} or u_*/C_p. Furthermore, that the spatial variability in R_{CD} never converged onto 1, at some distance cross-shore reflected that the transect never left the depth-limited regime of a portion of the wave band. This contrasts similarly aimed work presented in Ortiz-Suslow et al. (2015) and highlights the local dependence of this wind-wave-current interactions in the nearshore.

A final note on the C_D results. Direct and bulk estimates of the drag rely on stability corrections based on MOST. These corrections may become invalid under certain conditions (Grachev et al., 2018; Högström et al., 2013; Vickers & Mahrt, 1999). For this case study, the role of stability could not be meaningfully investigated due to the limited range of variance in ζ. Furthermore, the observations came from near-neutral conditions and so the stability corrections themselves were generally small (within 30%). However, the results of R_{CD} may change under various stability corrections and further investigations should be done to more generally characterize this dependence.

As a separate investigation, the measured u_* was compared to u_{*H}, both using the original Högström et al. (2015) formulae and a generalization of this to arbitrary water depths. In terms of order of magnitude, the original u_{*H} performed reasonably well, but the depth-limited equivalent substantially improved model-observation comparisons. Though not shown in the analysis presented here, u_{*H} was further modified to include the second-order effects in the dispersion relationship, but the results were negligibly different from the linear dispersion results. Even after generalizing the model, u_{*H} tended to underestimate the measurements. A significant portion of the residual variance in R_* was linked to MASL stability (both in a bulk and turbulent sense), sea state (both peak wave steepness and Urs), and the wind/stress directions. This stability dependence suggests that flow interaction with waves is dependent on the wave form as well as the fundamental characteristics of the turbulence in the MASL, which is not accounted for in the Högström model.

In general, R_* tended to increase over the sampling period, which coincided with the development of the local wind sea on top of the swell waves. This divergence was most likely driven by the assumption used to develop u_{*H}: of a wind sea riding on top of a quasi-monochromatic carrier swell wave. The wave field during 13 June was not this simple and further expanding this model to include mixed wave states and a more realistic ocean surface went beyond the scope of this study. These results were encouraging because they demonstrated that the measurements captured variability that could be represented by using a physically based model. This suggests that the results of the investigation into C_D highlight shortcomings in the parameterizations, rather than the measurements.

The analysis of the wind stress veering revealed that a shift occurred between the processes driving the wind stress angle in- and offshore of ~2 km. Within 2 km, the majority of the observations exhibited a strong relationship with the alongshore surface current variance ($r^2 > 0.72$). For transects I and IV, the wind stress veered to the south of the wind vector, which corresponded with a general *opposition* to the alongshore currents (flowing from north to south). Therefore, it maybe that some hydrodynamic forcing of the short waves at the surface caused the observed veering of the wind stress. Transect III exhibited the strongest relationship with the surface currents ($r^2 = 0.957$, $p < 0.05$), but the pattern differed from transect I and IV. Mainly, the strongest veering occured within 3 km of the beach and the stress angle tended to converge onto the wind direction, rather than away from it. Interestingly, this spatial pattern in the stress angle resembles the variability from transect II, where the wind had shifted to the southwest. However, in the case of transect III, the wind had already returned to roughly onshore. This may suggest that the transition between transects II and III captured a decoupling of the wind stress field from the wind velocity field. In other words, the spatial distribution of stress angles for transect III within this 2- to 3-km zone may have been driven by some processes all-together independent of the contemporaneous wind vector. For transect II, the wind stress angle exhibited a positive relationship with the surface currents, but the results were not found to be statistically significant, even within the 2-km zone. The same results held when testing II within 3-km. This may have resulted from II having the fewest number of overall samples.

Outside of the region with strong veering and current dependence, all of the transects exhibited a wind stress angle about 20° to the south of the azimuthal wind velocity vector. This consistent pattern may have been driven by the incident surface gravity waves. For the case of swell oblique to wind, the stress vector should lie

between the wind and swell directions (Grachev et al., 2003). For all of the CLASI data, the swell was oblique to the wind, but this mechanism was confused by the multiple swell systems into the MB during the observing period. A low-frequency, ~0.058-Hz, SW swell was incident into MB throughout all of 13 June (broadly centered on 235°), which would align these waves obliquely to the left of the shore normal and the wind direction. Therefore, the mean wind stress angle offshore of 2 km was consistently between the mean wind vector and this southerly swell. This was in spite of the *peak* swell being from WNW at 0.1–0.15 Hz. This somewhat counterintuitive finding may be attributed to the southerly swell shoaling in relatively deeper water, due to its longer wavelength, and thus having an earlier impact on the stress than the peak swell. Drawing more specific conclusions from these measurements is limited by the lack of local directional wave information across the transects.

6. Conclusions

The spatial and temporal variability of the air-sea momentum flux across a portion of the MB inner shelf has been investigated using simultaneous measurements of wind, waves, and currents made from a small, heavily instrumented research vessel. The primary aim of this study was to determine if the measured momentum flux could be predicted by bulk parameterizations of C_D and u_*. The observed C_D was compared to seven parameterizations, including: COARE 3.5 and two depth-limited drag models. In general, no parameterization was able to adequately capture the observed variance and in fact C_D was consistently underestimated by 2–4 times. A depth-limited surface roughness derived C_D, proposed by Jiménez and Dudhia (2018), performed the best with a mean 2.087 ($\pm$30%), which was substantially lower (20–30%) than all other models. Excluding the Jiménez and Dudhia (2018) model, there was operationally little difference between the wind speed-only-dependent COARE 3.5 and a depth-limited, sea state-dependent C_D.

A separate analysis was conducted on the friction velocity and off-wind stress angle. The directly measured u_* was compared to a bulk, wave-dependent parameterization (Högström et al., 2015). After generalizing the model to arbitrary water depths, the predicted value was within ~30% of the measured u_*. Latent, nonrandom variability was strongly associated with MASL stability and the relative directions of wind vector and stress to the ocean surface. Depth-limited wave nonlinearity only became important to the model-observation divergence for the latter half of sampling. These results are encouraging for the Högström u_* model, but also highlight that the underlying basis for this model, a wind sea on top of a psuedo-monochromatic swell, breaks down significantly in multimodel sea states. The wind stress angle analysis revealed a shift from a current- to swell-dominated veering mechanism inshore and offshore of ~2 km from the beach, respectively. Inshore of 2 km, the alongshore current gradients dominated the stress angle variance ($r^2 > 0.72$, all $p < 0.05$). However, offshore, a persistent wind stress 22.2° to the south of the wind vector was observed, which placed the stress vector between the wind and a southerly swell incident to MB.

The findings from this case study reinforce the complexity of air-sea interaction in the nearshore, especially for environments with strong hydrodynamic and swell forcing. While some of the variability can be captured by available models and parameterizations, significant gaps remain in understanding the driving the momentum flux in a depth-limited regime. Investigating the relationship between the wind stress and the directional spectrum of the short gravity-capillary waves may improve the predictability of coastal air-sea interaction. In particular, it may be necessary to better understand what portion of the short wave spectrum *holds* the stress and how this spatially evolves in frequency and direction contemporaneously with the shoaling long waves.

References

Anctil, F., & Donelan, M. (1996). Air-water momentum flux observations over shoaling waves. *Journal of Physical Oceanography*, *26*, 10.

Anctil, F., Donelan, M., Drennan, W., & Graber, H. (1994). Eddy-correlation measurements of air-sea fluxes from a discus buoy. *Journal of Atmospheric and Oceanic Technology*, *11*, 7.

Andreas, E., Mahrt, L., & Vickers, D. (2014). An improved bulk air-sea surface flux algorithm, including spray-mediated transfer. *Quarterly Journal of the Royal Meteorological Society*, *141*, 642–654. https://doi.org/10.1002/qj.2424

Charnock, H. (1955). Wind stress on a water surface. *Quarterly Journal of the Royal Meteorological Society*, *81*(350), 1.

Collins, C. O. I. (2012). In situ wave measurements: Sensor comparison and data analysis (Ph.D. thesis), University of Miami.

Collins, C. O., Blomquist, B., Persson, O., Lund, B., Rogers, W. E., Thomson, J., et al. (2017). Doppler correction of wave frequency spectra measured by underway vessels. *Journal of Atmospheric and Oceanic Technology*, *34*(2), 429–436. https://doi.org/10.1175/JTECH-D-16-0138.1

Cornillon, P., & Park, K.-A. (2001). Warm core ring velocities inferred from NSCAT. *Geophysical Research Letters*, *28*(4), 575–578. https://doi.org/10.1029/2000GL011487

Donelan, M. (1990). Air-sea interaction. In B. LeMehaute, & D. Hanse (Eds.), *The sea, vol. 9: Ocean engineering science*, Air-Sea In. Hoboken, N.J: John Wiley & Sons, Ltd., pp. 239–292.

Donelan, M. A., Curcic, M., Chen, S. S., & Magnusson, A. K. (2012). Modeling waves and wind stress. *Journal of Geophysical Research*, *117*, C00J23. https://doi.org/10.1029/2011JC007787

Donelan, M. A., Haus, B. K., Reul, N., Plant, W. J., Stiassnie, M., Graber, H. C., et al. (2004). On the limiting aerodynamic roughness of the ocean in very strong winds. *Geophysical Research Letters*, *31*, 5. https://doi.org/10.1029/2004gl019460

Drennan, W. M., Donelan, M. A., Madsen, N., Katsaros, K. B., Terray, E. A., & Flagg, C. N. (1994). Directional wave spectra from a swath ship at sea. *Journal of Atmospheric and Oceanic Technology*, *11*, 1109–1116.

Drennan, W. M., Graber, H. C., & Donelan, M. A. (1999). Evidence for the effects of swell and unsteady winds on marine wind stress. *Journal of Physical Oceanography*, *29*(8), 1853–1864. https://doi.org/10.1175/1520-0485

Drennan, W. M., Graber, H. C., Hauser, D., & Quentin, C. (2003). On the wave age dependence of wind stress over pure wind seas. *Journal of Geophysical Research*, *108*(C3), 8062. https://doi.org/10.1029/2000JC000715

Drennan, W. M., Kahma, K. K., & Donelan, M. A. (1999). On momentum flux and velocity spectra over waves. *Boundary-Layer Meteorology*, *92*(3), 489–515. https://doi.org/10.1023/A:1002054820455

Edson, J. B., Jampana, V., Weller, R. A., Bigorre, S. P., Plueddemann, A. J., Fairall, C. W., et al. (2013). On the exchange of momentum over the open ocean. *Journal of Physical Oceanography*, *43*(8), 22. https://doi.org/10.1175/jpo-d-12-0173.1

Fairall, C. W., Bariteau, L., Grachev, A. A., Hill, R. J., Wolfe, D. E., Brewer, W. A., et al. (2006). Turbulent bulk transfer coefficients and ozone deposition velocity in the international consortium for atmospheric research into transport and transformation. *Journal of Geophysical Research*, *111*, D23S20. https://doi.org/10.1029/2006JD007597

Geernaert, G. (1988). Drag coefficient modeling for the near coastal zone. *Dynamics of Atmospheres and Oceans*, *11*(3-4), 307–322. https://doi.org/10.1016/0377-0265(88)90004-8

Geernaert, G. L., Katsaros, K. B., & Richter, K. (1986). Variation of the drag coefficient and its dependence on sea state. *Journal of Geophysical Research*, *91*(C6), 7667. https://doi.org/10.1029/JC091iC06p07667

Goring, V. I., & Nikora, D. G. (2002). Despiking acoustic DOPPLER velocimeter data. *Journal of Hydraulic Engineering*, *128*(1), 10. https://doi.org/10.1061//asce/0733-9429/2002/128:1/117

Grachev, A. A., Bariteau, L., Fairall, C. W., Hare, J. E., Helmig, D., Hueber, J., & Lang, E. K. (2011). Turbulent fluxes and transfer of trace gases from ship-based measurements during TexAQS 2006. *Journal of Geophysical Research*, *116*, D13110. https://doi.org/10.1029/2010JD015502

Grachev, A. A., & Fairall, C. W. (2001). Upward momentum transfer in the marine boundary layer. *Journal of Physical Oceanography*, *31*(7), 1698–1711. https://doi.org/10.1175/1520-0485(2001)031<1698:UMTITM>2.0.CO;2

Grachev, A. A., Fairall, C. W., Hare, J. E., Edson, J. B., & Miller, S. D. (2003). Wind stress vector over ocean waves. *Journal of Physical Oceanography*, *33*(11), 2408–2429. https://doi.org/10.1175/1520-0485(2003)033<2408:WSVOOW>2.0.CO;2

Grachev, A. A., Leo, L. S., Fernando, H. J. S., Fairall, C. W., Creegan, E., Blomquist, B. W., et al. (2018). Air-sea/land interaction in the coastal zone. *Boundary-Layer Meteorology*, *167*(2), 181–210. https://doi.org/10.1007/s10546-017-0326-2

Högström, U., Sahlée, E., Smedman, A.-S., Rutgersson, A., Nilsson, E., Kahma, K. K., & Drennan, W. M. (2015). Surface stress over the ocean in swell-dominated conditions during moderate winds. *Journal of the Atmospheric Sciences*, *72*, 18. https://doi.org/10.1175/JAS-D-15-0139.1

Högström, U., Rutgersson, A., Sahlée, E., Smedman, A.-S., Hristov, T. S., Drennan, W. M., & Kahma, K. K. (2013). Air-sea interaction features in the Baltic Sea and at a Pacific trade-wind site: An inter-comparison study. *Quarterly Journal of the Royal Meteorological SocietyBoundary-Layer Meteorology*, *147*(1), 139–163. https://doi.org/10.1007/s10546-012-9776-8

Högström, U., Sahlée, E., Smedman, A.-S., Rutgersson, A., Nilsson, E., Kahma, K. K., & Drennan, W. M. (2018). The transition from downward to upward air-sea momentum flux in swell-dominated light wind conditions. *Journal of the Atmospheric Sciences*, *75*(8), 2579–2588. https://doi.org/10.1175/JAS-D-17-0334.1

Holthuijsen, L. (2007). *Waves in oceanic and coastal waters* (1st ed.). New YorkNew York: Cambridge University Press.

Janssen, P. A. E. M. (1989). Wave-induced stress and the drag of air flow over sea waves. *Journal of Physical Oceanography*, *19*(6), 745–754. https://doi.org/10.1175/1520-0485(1989)019<0745:WISATD>2.0.CO;2

Jiménez, P. A., & Dudhia, J. (2018). On the need to modify the sea surface roughness formulation over shallow waters. *Journal of Applied Meteorology and Climatology*, *57*(5), 1101–1110. https://doi.org/10.1175/JAMC-D-17-0137.1

Kahma, K. K., Donelan, M. A., Drennan, W. M., Terray, E. A., Kahma, K. K., Donelan, M. A., et al. (2016). Evidence of energy and momentum flux from swell to wind. *Journal of Physical Oceanography*, *46*(7), 2143–2156. https://doi.org/10.1175/JPO-D-15-0213.1

Kitaigorodskii, S., & Volkov, Y. A. (1965). On the roughness parameter of the sea surface and the calculation of momentum flux in the near-water layer of the atmosphere. *Izvestiya, Atmospheric and Oceanic Physics*, *1*, 973–988.

Large, W., & Pond, S. (1981). Open ocean momentum flux measurements in moderate to strong winds. *Journal of Physical Oceanography*, *11*, 13.

MacMahan, J. (2017). Increased aerodynamic roughness owing to surfzone foam. *Journal of Physical Oceanography*, *47*(8), 2115–2122. https://doi.org/10.1175/JPO-D-17-0054.1

Mahrt, L., Vickers, D., Howell, J., Højstrup, J., Wilczak, J. M., Edson, J., & Hare, J. (1996). Sea surface drag coefficients in the Risø air sea experiment. *Journal of Geophysical Research*, *101*(C6), 14,327–14,335. https://doi.org/10.1029/96JC00748

Monin, A., & Obukhov, A. (1954). Basic laws of turbulent mixing in the surface layer of the atmosphere. *Tr. Akad Nauk SSSR Geophiz*, *24*(151), 30.

National Geophysical Data Center (2016). U.S. Coastal Relief Model—Southern California. https://doi.org/doi:10.7289/V500001J

Niaki, S. T. A., & Abbasi, B. (2007). Skewness reduction approach in multi-attribute process monitoring. *Communications in Statistics-Theory and Methods*, *36*(12), 2313–2325. https://doi.org/10.1080/03610920701215456

Ortiz-Suslow, D. G., Haus, B. K., Williams, N. J., Laxague, N. J. M., Reniers, A. J. H. M., & Graber, H. C. (2015). The spatial-temporal variability of air-sea momentum fluxes observed at a tidal inlet. *Journal of Geophysical Research: Oceans*, *120*, 660–676. https://doi.org/10.1002/2014JC010412

Potter, H. (2015). Swell and the drag coefficient. *Ocean Dynamics*, *65*(3), 375–384. https://doi.org/10.1007/s10236-015-0811-4

Potter, H., Graber, H. C., Williams, N. J., Collins, C. O., Ramos, R. J., & Drennan, W. M. (2015). In situ measurements of momentum fluxes in typhoons. *Journal of the Atmospheric Sciences*, *72*, 104–118. https://doi.org/10.1175/JAS-D-14-0025.1

Prandtl, L. (1925). Bericht über Untersuchungen zur ausgebildeten turbulenz. *Zeitschrift für Angewandte Mathematik und Mechanik*, *5*(2), 136–139.

Rieder, K. F. (1997). Analysis of sea-surface drag parameterizations in open ocean conditions. *Boundary-Layer Meteorology*, *82*(3), 355–377. https://doi.org/10.1023/A:1000289415922

Shabani, B., Nielsen, P., & Baldock, T. (2014). Direct measurements of wind stress over the surf zone. *Journal of Geophysical Research: Oceans*, *119*, 2949–2973. https://doi.org/10.1002/2013JC009585

Smedman, A., Högström, U., Bergström, H., Rutgersson, A., Kahma, K. K., & Pettersson, H. (1999). A case study of air-sea interaction during swell conditions. *Journal of Geophysical Research*, *104*(C11), 25833. https://doi.org/10.1029/1999jc900213

Smith, S. D. (1980). Wind stress and heat flux over the ocean in gale force winds. *Journal of Physical Oceanography*, *10*, 18.

Smith, S. D. (1988). Coefficients for sea surface wind stress, heat flux, and wind profiles as a function of wind speed and temperature. *Journal of Geophysical Research*, *93*(C12), 15467. https://doi.org/10.1029/JC093iC12p15467

Smith, S. D., & Banke, E. G. (1975). Variation of the sea surface drag coefficient with wind speed. *Quarterly Journal of the Royal Meteorological Society*, *101*, 8.

Tennekes, H., & Lumley, J. (1972). *A first course in turbulence*: MIT Press.

Ursell, F. (1953). The long-wave paradox in the theory of gravity waves. *Mathematical Proceedings of the Cambridge Philosophical Society*, *49*(4), 685. https://doi.org/10.1017/S0305004100028887

Vickers, D., & Mahrt, L. (1999). Observations of non-dimensional wind shear in the coastal zone. *Quarterly Journal of the Royal Meteorological Society*, *125*, 2685–2702.

Zhang, F. W., Drennan, W. M., Haus, B. K., & Graber, H. C. (2009). On wind-wave-current interactions during the shoaling waves experiment. *Journal of Geophysical Research*, *114*, 12. https://doi.org/10.1029/2008jc004998

Zhao, Z. K., Liu, C. X., Li, Q., Dai, G. F., Song, Q. T., & Lv, W. H. (2015). Typhoon air-sea drag coefficient in coastal regions. *Journal of Geophysical Research: Oceans*, *120*, 716–727. https://doi.org/10.1002/2014JC010283